

The first exploration of the correlations between *WISE* 12 μm and CO emission in early-type galaxies

YANG GAO,^{1,2} ENCI WANG,³ QING-HUA TAN,⁴ TIMOTHY A. DAVIS,⁵ FU-HENG LIANG,^{6,7} XUE-JIAN JIANG,⁸ NING GAI,¹ QIAN JIAO,⁹
DONGDONG SHI,¹⁰ SHUAI FENG,^{11,12,13} YANKE TANG,¹ SHIJIE LI,¹ AND YI-FAN WANG¹

¹College of Physics and Electronic Information, Dezhou University, Dezhou 253023, China

²International Centre of Supernovae, Yunnan Key Laboratory, Kunming 650216, China

³CAS Key Laboratory for Research in Galaxies and Cosmology, Department of Astronomy, University of Science and Technology of China, Hefei 230026, People's Republic of China

⁴Purple Mountain Observatory, Chinese Academy of Sciences, 10 Yuanhua Road, Nanjing 210023, China

⁵Cardiff Hub for Astrophysics Research & Technology, School of Physics & Astronomy, Cardiff University, Queens Buildings, Cardiff CF24 3AA, UK

⁶European Southern Observatory (ESO), Karl-Schwarzschild-Straße 2, 85748 Garching, Germany

⁷Sub-department of Astrophysics, Department of Physics, University of Oxford, Denys Wilkinson Building, Keble Road, Oxford OX1 3RH, UK

⁸Research Center for Astronomical Computing, Zhejiang Laboratory, Hangzhou 311121, China

⁹School of Electrical and Electronic Engineering, Wuhan Polytechnic University, Wuhan 430023, China

¹⁰Center for Fundamental Physics, School of Mechanics and Optoelectric Physics, Anhui University of Science and Technology, Huainan, Anhui 232001, People's Republic of China

¹¹College of Physics, Hebei Normal University, 20 South Erhuan Road, Shijiazhuang 050024, People's Republic of China

¹²Guoshoujing Institute of Astronomy, Hebei Normal University, 20 South Erhuan Road, Shijiazhuang 050024, People's Republic of China

¹³Hebei Key Laboratory of Photophysics Research and Application, Shijiazhuang 050024, People's Republic of China

(Received; Revised; Accepted)

Submitted to ApJ

ABSTRACT

We present the analysis of a comprehensive sample of 352 early-type galaxies using public data, to investigate the correlations between CO luminosities and mid-infrared luminosities observed by *Wide-field Infrared Survey Explorer* (*WISE*). We find strong correlations between both CO (1-0) and CO (2-1) luminosities and 12 μm luminosity, boasting a correlation coefficient greater than 0.9 and an intrinsic scatter smaller than 0.1 dex. The consistent slopes observed for the relationships of CO (1-0) and CO (2-1) suggest that the line ratio R_{21} lacks correlation with mid-infrared emission in early-type galaxies, which is significantly different from star-forming galaxies. Moreover, the slopes of $L_{\text{CO}(1-0)}-L_{12\mu\text{m}}$ and $L_{\text{CO}(2-1)}-L_{12\mu\text{m}}$ relations in early-type galaxies are steeper than those observed in star-forming galaxies. Given the absence of correlation with color, morphology or sSFR, the correlation between deviations and the molecular gas mass surface density could be eliminated by correcting the possible 12 μm emission from old stars or adopting a systematically different α_{CO} . The latter, on average, is equivalent to adding a constant CO brightness density, specifically $2.8^{+0.8}_{-0.6}$ [K km s^{-1}] and $4.4^{+2.2}_{-1.4}$ [K km s^{-1}] for CO (1-0) and (2-1) respectively. These explorations will serve as useful tools for estimating the molecular gas content in gas-poor galaxies and understanding associated quenching processes.

Keywords: galaxies: evolution – galaxies: ISM – galaxies: molecular gas – galaxies: infrared photometry – galaxies: elliptical and lenticular, cD

1. INTRODUCTION

Modern galaxy formation models suggest that within dark matter halos, gas cools and collapses to form stars, a process facilitated by high gas densities and effective dust shielding from intense and hard radiation fields (Visser et al. 2009; Wolfire et al. 2010, 2022). Observations reveal that stars predominantly form from dusty molecular interstellar gas, as demonstrated by the strong correlation between the surface densities of the star formation rate (SFR) and molecular gas

Corresponding author: Yang Gao
gao14681@mail.ustc.edu.cn

Corresponding author: Enci Wang
ecwang16@ustc.edu.cn

(H₂), rather than atomic gas (Baan et al. 2008; Bigiel et al. 2008; Leroy et al. 2008). Furthermore, a tighter correlation exists between SFRs, traced by infrared luminosity, and dense molecular gas masses, as indicated by HCN emission (Gao & Solomon 2004a,b).

Star formation is a multifaceted process influenced not only by the intrinsic properties of galaxies and their external environments—ranging from local to large-scale conditions (Peng et al. 2010; Kauffmann et al. 2006; Li et al. 2012)—but also by physical conditions on subkiloparsec scales (Krumholz & McKee 2005). To fully unravel the mechanisms driving galaxy evolution, it is crucial to explore the interplay between stars and gas across extensive and diverse samples of galaxies.

Molecular gas masses are commonly derived from the flux of ¹²CO (hereafter CO) millimeter low rotational (J) lines using the "conversion factor" α_{CO} (Solomon et al. 1987; Bolatto et al. 2013). However, this conversion factor depends on several physical parameters, including metallicity, gas density, and temperature, and can vary by up to an order of magnitude (Bolatto et al. 2013; Accurso et al. 2017; Tacconi et al. 2020). Additionally, the size of CO samples remains significantly smaller than those of optical surveys due to sensitivity limitations and other observational uncertainties. As an alternative, gas masses can be estimated from dust masses using a metallicity-dependent gas-to-dust ratio (δ_{GDR}) (Leroy et al. 2011; Draine & Li 2007). This dust-based approach accounts for not only molecular gas but also a portion of atomic hydrogen present in the H₂-dominant molecular gas disk (Bertemes et al. 2018).

Building on this, we proposed that molecular gas masses for large galaxy samples can be estimated using a single mid-infrared (mid-IR) band measurement, specifically the 12 μm luminosity from the full-sky survey conducted by the Wide-field Infrared Survey Explorer (WISE) (Jiang et al. 2015; Gao et al. 2019). The strong and tight correlation between CO emission and 12 μm luminosity has been established using hundreds of global galaxies and is further confirmed at subkiloparsec scales (Chown et al. 2021; Gao et al. 2022) and in extensive galaxy samples (Leroy et al. 2023a). However, these studies include only a small number of early-type galaxies (ETGs), most of which are non-detections. Consequently, we refer to the CO (1-0) and CO (2-1) relations derived by Gao et al. (2019) as representative of typical star-forming global galaxy populations.

Although the relationship between mid-IR and CO rotational line emission is among the strongest scaling relations in extragalactic astronomy (Leroy et al. 2023a), it can vary significantly across galaxies. These variations may depend on galaxy properties such as stellar mass (M_*) and specific star formation rate (SFR/ M_*), potentially introducing offsets and uncertainties in molecular gas mass estimates for certain systems. Addressing this issue is critical, particularly as high-

resolution and high-sensitivity ISM maps from widespread mid-IR observations, including those at high redshift, become increasingly accessible with the successful commissioning of the James Webb Space Telescope (JWST; Rieke et al. 2015). In this work, we for the first time explore this scaling-relation for early-type galaxies, and further investigate the dependence on galaxy properties.

The WISE 12 μm band spans wavelengths from 7.5 to 16.5 μm (Jarrett et al. 2011), capturing a blend of prominent polycyclic aromatic hydrocarbon (PAH) feature emissions (Draine & Li 2007) and continuum emissions from stochastically heated small dust grains (Wright et al. 2010). PAH carriers are spatially mixed to varying degrees with cold dust and molecular gas (Churchwell et al. 2006; Bendo et al. 2008, 2010; Sandstrom et al. 2010, 2012). These molecules absorb ionizing UV photons from H II regions and re-emit infrared radiation through features like C–H bending and C–C stretching, contributing up to 20% of a galaxy’s total infrared power (Smith et al. 2007; Diamond-Stanic & Rieke 2010). Additionally, heating within photodissociation regions can dissipate via collisionally excited rotational-vibrational H₂ lines and rotational transitions of other abundant molecules (Meijerink & Spaans 2005). Consequently, on scales ranging from kiloparsecs to integrated galaxies, PAH emissions exhibit a strong association with molecular gas tracers such as CO (Cortzen et al. 2019).

The mid-IR continuum emission from dust grains primarily responds to UV radiation from young stars, though contributions from older stellar populations can dominate in some cases (Leroy et al. 2012; Boquien et al. 2016). Observations suggest that PAH emission is more closely correlated with molecular gas tracers such as CO than the mid-IR continuum alone (Leroy et al. 2023b; Whitcomb et al. 2023). In ETGs, where star formation is minimal or absent (Yi et al. 2005; Kaviraj et al. 2007), 12 μm emission from the circumstellar material heated by post-AGB stars may become significant (Davis et al. 2014), with morphology playing a key role in determining mid-IR properties (Temi et al. 2009). These galaxies, often rich in hot gas but with low star formation efficiency (O’Sullivan et al. 2001), provide a unique environment to study the relative contributions of PAH features, dust continuum, and CO-dark gas (Chastenet et al. 2019; Leroy et al. 2019).

Our paper is structured as follows. In Section 2, we describe the sample and data used in this paper. In Section 3, we present the results about correlations between CO and WISE 12 μm luminosities for ETGs, and examine their dependence on galaxy properties. In Section 4 we attempt to explain physical origin of the higher slope in ETGs, and make two relevant preliminary test in Appendix A and B. Finally, we summarize our findings in Section 5.

2. SAMPLE AND DATA

2.1. CO Data

To maximize the sample size for studying the relationships between CO and mid-IR emission, it is essential to gather CO data for as many ETGs as possible, given the limited availability of CO observations compared to the all-sky coverage of 12 μm data. To minimize biases due to incompleteness, most of our ETGs (317 out of 352) are drawn from two volume-limited surveys: ATLAS3D (Young et al. 2011), which includes galaxies with $M_K < -21.5$ and distances < 42 Mpc, and MASSIVE (Ma et al. 2014; Davis et al. 2019), targeting galaxies within 108 Mpc and $M_K < -25.3$. To supplement this dataset, we incorporate CO measurements from the statistically complete samples of nearby group E/S0 galaxies in SAURON (Combes et al. 2007) and group-dominant ETGs in CLoGS (O’Sullivan et al. 2018), along with CO (1-0) and CO (2-1) luminosities of four dwarf S0 galaxies from Ge et al. (2021) observed with the IRAM 30-m telescope.

For galaxies with overlapping CO measurements across these surveys, we prioritize data with higher signal-to-noise ratios, detections over non-detections, and stricter upper limits where applicable. In total, as shown in Table B, we obtain 82 CO (1-0) and 76 CO (2-1) detections with signal-to-noise ratio $S/N \geq 3$, and use 5 times the uncertainty as upper limits for non-detections¹. Most of the CO (1-0) and CO (2-1) intensities in our dataset were measured with the IRAM 30-m telescope, but the conversion factors from intensity to flux density differ across the original referenced papers. To ensure consistency, we adopt a standard conversion factor of 4.73 Jy K^{-1} to normalize all IRAM 30-m observations at both frequencies in our sample (Young et al. 2011). Finally, we calculate the CO line luminosities in units of $[\text{K km s}^{-1} \text{ pc}^2]$ using the formula provided by Bolatto et al. (2013):

$$\left(\frac{L_{\text{CO}}}{\text{K km s}^{-1} \text{ pc}^2}\right) = 2453 \left(\frac{S_{\text{CO}} \Delta\nu}{\text{Jy km s}^{-1}}\right) \left(\frac{D_L}{\text{Mpc}}\right)^2 (1+z)^{-1}. \quad (1)$$

2.2. WISE 12 μm Luminosity

The W3 luminosities in CO (1-0) and CO (2-1) beams are denoted as $L_{12\mu\text{m}(1-0)}$ and $L_{12\mu\text{m}(2-1)}$, as shown in Table B. We calculated the 12 μm luminosities based on the WISE band 3 flux and uncertainty maps downloaded from the NASA/IPAC Infrared Science Archive (WISE Team 2020), following the methodology outlined in Chown et al. (2021) and Gao et al. (2022).

The detailed reduction process for the 12 μm data is as follows. Background maps were estimated and subtracted using the SExtractor package (Bertin & Arnouts 1996). During this step, we derived the WISE 12 μm magnitudes ($mag_{12\mu\text{m}}$) and their instrumental uncertainties for galaxies with CO measurements taken by interferometers. For galaxies observed with single-dish telescopes, the background-subtracted flux and uncertainty images were convolved to match the Gaussian point spread function (PSF) corresponding to the CO beam sizes. In 12 μm maps, the flux ($F_{12\mu\text{m}}$) is in units of digital numbers (DN), where 1 DN corresponds to 18.0 mag (zero-point magnitude), and zero magnitude attributes isophotal frequency equivalent flux density 31.674 Jy (S_0 , Jarrett et al. 2011). The flux density in Jy is calculated as:

$$\begin{aligned} S_{12\mu\text{m}}/\text{Jy} &= 31.674 \times 10^{-0.4mag} \\ &= 1.998 \times 10^{-6} F_{12\mu\text{m}}/\text{DN}. \end{aligned} \quad (2)$$

For flux density measurements within the CO beams, a correction factor of $1.133 \times (\text{beam size}/\text{pixel size})^2$ was applied. The 12 μm luminosity was then computed using the formula:

$$L_{12\mu\text{m}}/L_{\odot} = 4\pi D_L^2 \Delta\nu S_{12\mu\text{m}}/\text{Jy}, \quad (3)$$

where the bandwidth $\Delta\nu$ is $1.1327 \times 10^{13} \text{ Hz}$ in the 12 μm band. The total uncertainty in $L_{12\mu\text{m}}$ was derived from the smoothed, background-subtracted flux and uncertainty images, incorporating instrumental uncertainty and a 4.5% zero-point uncertainty in quadrature, following a methodology similar to Appendix A of Chown et al. (2021).

2.3. Galaxy-integrated parameters

The morphological T types, which classify galaxies based on spiral arm strength and ellipticity (Pan et al. 2022), were obtained for 346 galaxies from the 2MASS Redshift Survey dataset (Huchra et al. 2012). For the remaining six targets, the classifications for NGC7693, PGC029321, and PGC061468 were taken from the ATLAS3D project (Cappellari et al. 2011). PGC35225 and PGC44685 were identified as dwarf S0 galaxies based on their visual morphologies and B-band magnitudes, as discussed in Ge et al. (2021). The classification of NGC2292 was sourced from de Vaucouleurs et al. (1991) and is available via the HyperLeda database².

Additional parameters displayed in the Figure 1, such as stellar masses, color and Sersic index, are taken from the NASA Sloan Atlas (NSA), which is a catalog of images and parameters for SDSS galaxies with $z < 0.15$ (Blanton et al. 2011).

Almost all the sample galaxies have T type < 0 with only 12 exceptions, which are also identified as ETGs using high-

¹ These CO non-detections include galaxies with measured fluxes less than three times their uncertainty (σ), even extending to negative values. Additionally, adopting different upper limits between 2 and 5σ does not significantly alter the slopes of these scaling relations or affect subsequent conclusions.

² <http://atlas.obs-hp.fr/hyperleda/>

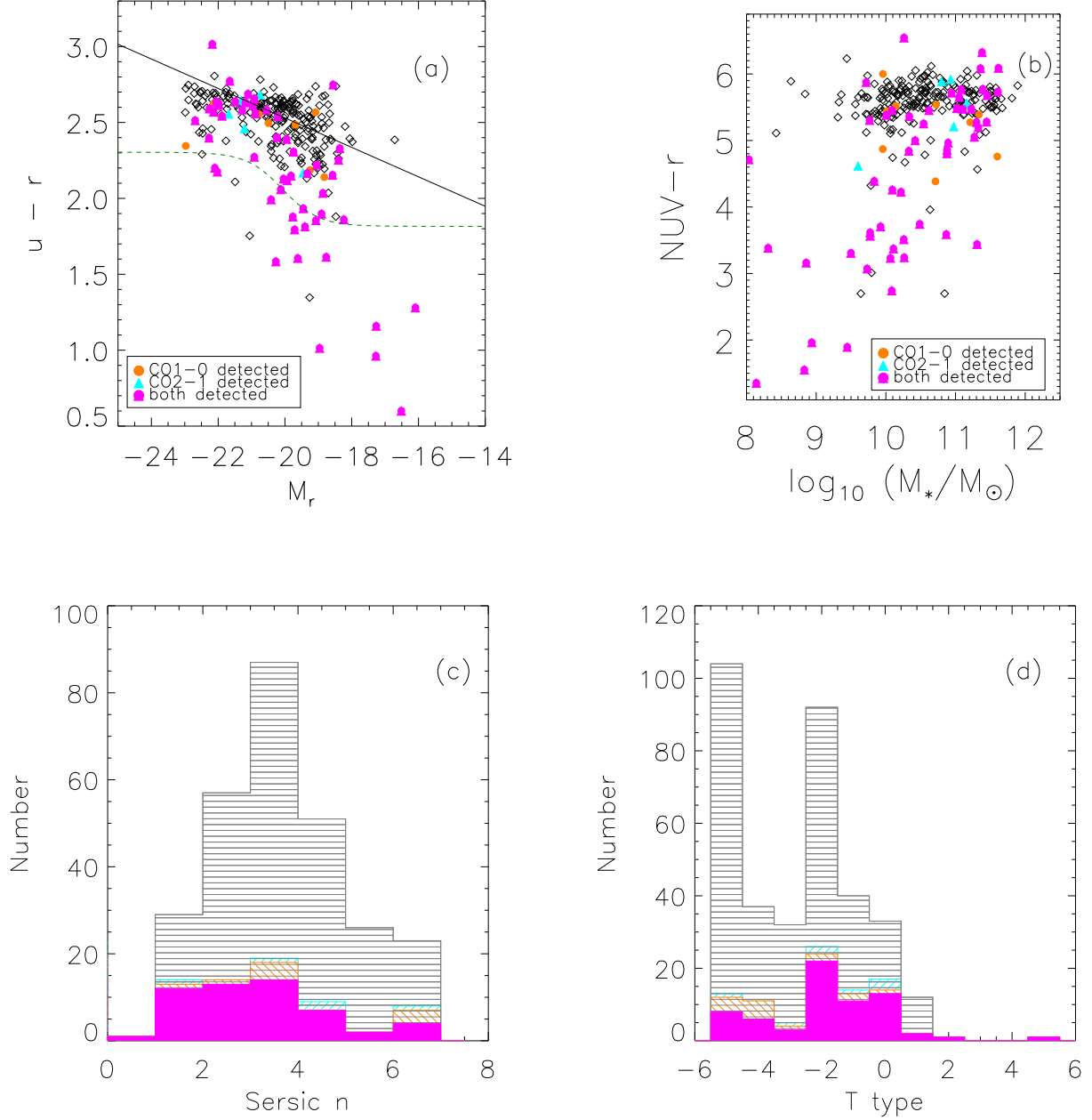


Figure 1. The panels show the distribution of our ETGs: the M_r versus $u-r$ colour–magnitude diagram shown in panel a, the stellar mass (M_*) vs. near-UV $-r$ plane in panel b, and the Sersic index (n) in panel c. These three panels are plotted based on the data of the subsample of 274 galaxies, using SDSS photometric parameters from NSA. Panel d displays the morphological T type distribution of the entire sample (352 galaxies). In panel a, the black line denotes the narrow early-type sequence computed by Cappellari et al. (2011), while the dashed line indicate the optimal divider between red sequence and blue cloud, as established by Baldry et al. (2004). The orange (circle), cyan (triangle) and magenta (circle + triangle) represents detection of only CO (1-0), only CO (2-1), and both, respectively, while the black diamonds and histograms correspond to non-detections.

quality imaging in ATLAS3D. This subset does not significantly affect our fitting results or conclusions. Most of these ETGs are also red, as shown in Figure 1, although the sample selection is based on morphology rather than color. For galaxies with CO (1-0 or 2-1) detections, over 77% have a Sersic index (n) ≥ 2 , about 75% fall within the red sequence based on their M_r and $u - r$ colors, and roughly 72% have near- $UV - r$ values greater than 4. The star-formation activity in these ETGs spans a wide range, differing significantly from that in star-forming galaxies, making this sample suitable for examining whether the correlation between 12 μm and CO emission is influenced by galaxy properties.

We compute the SFR for galaxies with detected IRAS 60 and 100 μm luminosities, using the calibrations of Sanders & Mirabel (1996) and Kennicutt (1998), assuming the Salpeter (1955) initial mass function.

3. RESULTS

3.1. The $L_{\text{CO}} - L_{12\mu\text{m}}$ correlations in ETGs

Figure 2 shows our most basic result, a power law (linear in logarithmic scale) correlation between the 12 μm luminosities and the detected CO luminosities in ETGs, though they are from different surveys.

We employ a Bayesian linear regression named *LinMix*³ (Kelly 2007), to take into account the uncertainties in both the L_{CO} and $L_{12\mu\text{m}}$. The Spearman's correlation coefficient (r) is 0.91 and 0.92 and the intrinsic scatter is 0.09 and 0.1 dex for CO(1-0) and CO(2-1) as listed in Table 1. The tightness and correlation is almost comparable to the relation measured based on the strongest star-forming galaxies (MALATANG; Gao et al. 2022), although the sample of ETGs is much smaller. So, assuming the galactic conversion factor $\alpha_{\text{CO}} = 3.2 M_{\odot} (\text{K km s}^{-1} \text{pc}^2)^{-1}$, the molecular gas mass in ETGs can be estimated using:

$$\log\left(\frac{M_{\text{mol}}}{\text{K km s}^{-1} \text{pc}^2}\right) = (1.14 \pm 0.06) \log\left(\frac{L_{12\mu\text{m}}}{L_{\odot}}\right) - (1.08 \pm 0.50). \quad (4)$$

3.2. Steeper CO vs. 12 μm slopes in ETGs

In Figure 2, we find the best fitting relations of ETGs (represented by the dark red lines) are steeper than the results (indicated by the green lines) based on the global sample of normal galaxies as performed by Gao et al. (2019).

However, the relative distribution of ETGs and normal SFGs differs in the two panels. In the left panel, at high-luminosity end, the ETGs locate in the same region indicated by the green line. But as luminosity decreases, they deviate significantly below this line, which suggests that as the 12 μm emission diminishes, the CO(1-0) emission weakens further. In the right panel, the deviation between the two 12 μm vs. CO(2-1) correlations of ETGs and normal SFGs

shows an opposite trend compared to the CO(1-0) deviation trend shown in the left panel. Thus, it seems plausible that compared to the (extrapolated) normal galaxy sample, at a given 12 μm luminosity, ETGs have lower CO(1-0) but higher CO(2-1) luminosity. This kind of difference can be naturally explained by the effects of beam size on the CO (2-1) to CO (1-0) lines ratio R_{21} (typically central enhancement; Sakamoto et al. 1994; Yajima et al. 2021; Leroy et al. 2022). By adopting higher R_{21} in SFGs, we can obtain similar trend of the deviation between ETGs and normal SFGs in the right panel as in the left panel.

So we focus more on the fitted slope of ETGs, which is slightly higher than that of SFGs for both CO(1-0) and CO(2-1). The literature comparison presented in the left panel includes the correlations between CO(1-0) and WISE 3 band luminosity measured in Gao et al. (2019), Chown et al. (2021) and Zhang & Ho (2023). In the right panel, beside the direct linking between CO(2-1) and 12 μm luminosity, we also show the correlations between CO and PAH emission as provided by Chown et al. (2024) and Shivaei & Boogaard (2024). Notably, the detected ETGs exhibit a correlation most closely resembling that observed in the diffuse regions of nearby star-forming galaxies (outside of centers and not covered by the nebular region mask), which imply these conditions are similar.

We directly compare the slopes of the correlations with CO(1-0) and CO(2-1) using the same sample. Specifically, based on 68 galaxies with detected emissions in both transitions, the slopes of the relations are nearly identical, measuring 1.16 ± 0.06 for CO(1-0) and 1.16 ± 0.07 for CO(2-1). This is different from the $R_{21} \propto I_{\text{MIR}}^{0.2}$ relation statistically inferred by Gao et al. (2019) and Leroy et al. (2023a), which is explained by the variation in R_{21} with the local SFR surface density in local star-forming or disk galaxies (den Brok et al. 2021; Yajima et al. 2021; Leroy et al. 2022). These discrepancy maybe a hint that the excitation condition of CO molecular rotational transitions is different in star-forming and early-type galaxies due to low star-formation activity, or indicate that the relation between 12 μm luminosity and SFR change in ETGs because the old stars can also contribute the MIR emission.

In Figure 2, the 5- σ CO upper limits for non-detections are close to the best-fitting line for detections, suggesting that these non-detections fall significantly below the fit. Consequently, including these non-detections in the analysis could substantially alter the best-fit parameters, as shown in Table 1⁴. Under similar observational depths, non-detection might signify samples with distinct physical properties (i.e. weaker

³ Obtainable from the NASA IDL Astronomy User's Library https://idlastro.gsfc.nasa.gov/ftp/pro/math/linmix_err.pro

⁴ We use *LinMix* Kelly (2007) and a new method provided by Jing & Li (2024) to do fitting and get similar results, suggesting that the differences should be from the data themselves.

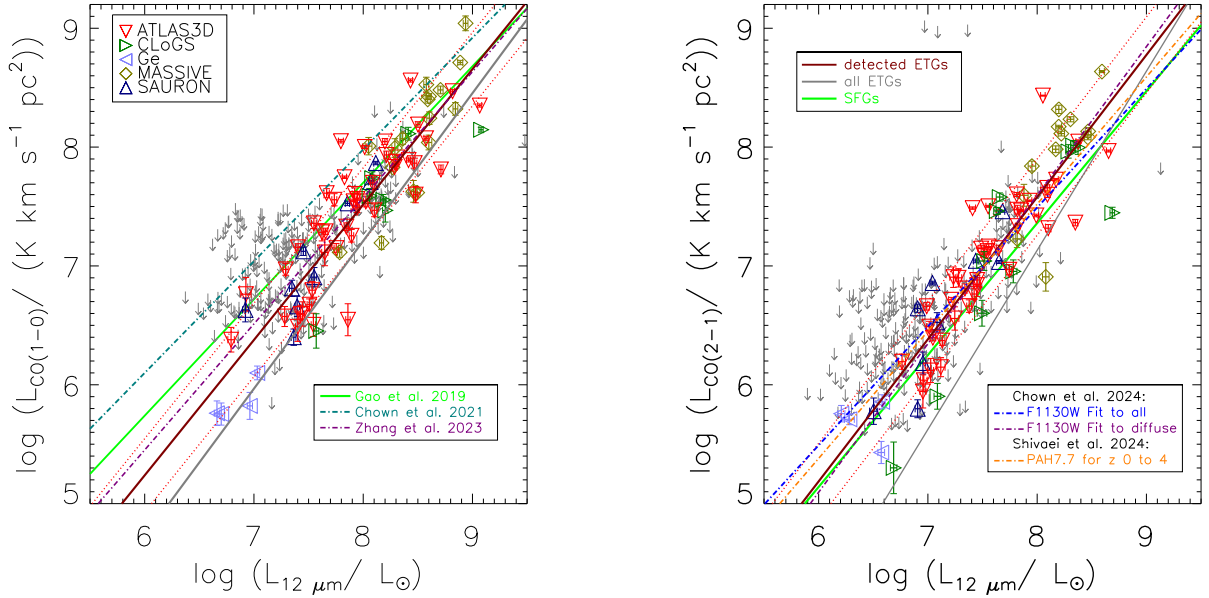


Figure 2. Correlations between the CO (1-0) and CO (2-1) luminosities and the mid-infrared monochromatic luminosities ($L_{12\mu\text{m}}$) as measured in the *WISE* 12 μm band for early-type galaxies. As indicated in the upper left corner, different colors and symbols represent detections from various CO projects, with error bars showing their respective measurement uncertainties. The dark gray downward-pointing arrows mean $5\text{-}\sigma$ CO upper limits. The dark red solid line and two dotted red lines respectively are the best-fitting linear relation (with parameters listed in Table 1) and the 1σ total/observed scatter for detections, and the grey line shows the fit when considering upper limits. In the left panel, we compile the best-fitting between $L_{12\mu\text{m}}$ and $L_{\text{CO}(1-0)}$ based on various samples for comparison: the green line is global (galaxy-wide) relation (Gao et al. 2019), the blue dot-dashed line indicates spatially resolved one in nearby star-forming galaxies (Chown et al. 2021), the purple line shows spatially resolved one in nearby star-forming galaxies and low-luminosity AGNs (Zhang & Ho 2023). In the right panel, we display the correlation between CO (2-1) and W3 band luminosity, and the ‘adjusted’ correlations between CO (2-1) and PAH (F1130W and 7.7 μm) luminosity with the slopes measured based on all pixels (blue) and diffuse regions (purple) at 50 – 150 pc scales in 66 nearby galaxies (Chown et al. 2024), and main sequence galaxies at redshifts ranging from 0 to 4 (Shivaei & Boogaard 2024).

CO) as our assumptions in APPENDIX A, and some of these non-detections maybe hint at a special galaxy evolutions.

3.3. No significant influence of global galaxy properties

It remains to be determined whether the slightly varying slopes observed in SFGs and ETGs would impact the efficacy of using the broadband *WISE* 12 μm band as a highly efficient alternative for estimating molecular gas mass. Consequently, our investigation focuses on examining how deviations correlate with representative quantities that are usually used to separate early-type and star-forming galaxies, such as color, morphology, stellar mass, and specific star formation rate (sSFR).

Variations in these parameters, such as dust attenuation and morphology, may imply the PAH excitation (12 μm emission) is linked with different stellar populations (Bendo et al. 2020). Notably, as the sSFR declines, the prominence of IR emission originating from recent star-forming activities lessens, while the contribution of dust heating by older stellar populations becomes more significant. This kind of analysis is the unique advantage of the ETG sample, enabling the exploration about

the link the *WISE* 12 micron emission and molecular gas content under this specific conditions.

Based on Figure 2, we then define the parameters $\Delta \log(L_{\text{CO}(1-0)})$ and $\Delta \log(L_{\text{CO}(2-1)})$ to characterise the deviation (overestimation or underestimation) of a given galaxy from the best-fitting relation of SFGs, follow the similar method in Gao et al. (2022):

$$\begin{aligned} \Delta \log(L_{\text{CO}}) &\equiv \log(L_{\text{CO,obs}}) - \log(L_{\text{CO,est}}), \\ \log\left(\frac{L_{\text{CO}(1-0),\text{est}}}{\text{K km s}^{-1} \text{ pc}^2}\right) &= 0.98 \log\left(\frac{L_{12\mu\text{m}}}{L_{\odot}}\right) - 0.14, \\ \log\left(\frac{L_{\text{CO}(2-1),\text{est}}}{\text{K km s}^{-1} \text{ pc}^2}\right) &= 1.11 \log\left(\frac{L_{12\mu\text{m}}}{L_{\odot}}\right) - 1.52. \end{aligned} \quad (5)$$

As shown in Figure 3, there is no dependence of these deviations on global properties of the host galaxies: NUV- r color, T type, or even sSFR. Consequently, the empirical predictor presented in Gao et al. (2019) remains applicable for estimating CO luminosity and molecular gas content in ETGs, albeit with increased scatter and a systematic offset, and the offset should be corrected without any other information (as shown in Appendix B).

Table 1. Summary of best-fit Relations.

Data Pair (y versus x)	Number of galaxies		k	b	Scatter		r	Figure
	Detections	Upper limits			σ_{tot}	σ_{int}		
(1)	(2)	(3)	(4)	(5)	(6)	(7)	(8)	(9)
$\log(L_{\text{CO}(1-0)})$ versus $\log L_{12\mu\text{m}}$	82	0	1.14 ± 0.06	-1.59 ± 0.50	0.31	0.09	0.91 ± 0.02	Left panel, Figure 2
$\log(L_{\text{CO}(1-0)})$ versus $\log L_{12\mu\text{m}}$	82	258	1.24 ± 0.07	-2.72 ± 0.52	0.31	0.16	0.87 ± 0.02	Left panel in Figure 2
$\log(L_{\text{CO}(2-1)})$ versus $\log L_{12\mu\text{m}}$	76	0	1.19 ± 0.06	-2.00 ± 0.49	0.32	0.10	0.92 ± 0.02	Right panel in Figure 2
$\log(L_{\text{CO}(2-1)})$ versus $\log L_{12\mu\text{m}}$	76	262	1.52 ± 0.10	-4.86 ± 0.78	0.37	0.10	0.82 ± 0.02	Right panel in Figure 2
galaxies with both CO (1-0) and (2-1) detections								
$\log(L_{\text{CO}(1-0)})$ versus $\log L_{12\mu\text{m}}$	68	0	1.16 ± 0.06	-1.72 ± 0.52	0.28	0.08	0.92 ± 0.02	
$\log(L_{\text{CO}(2-1)})$ versus $\log L_{12\mu\text{m}}$	68	0	1.16 ± 0.07	-1.69 ± 0.54	0.32	0.10	0.92 ± 0.02	

NOTE—The rows display the best-fitting linear relations of L_{CO} [$\text{K km s}^{-1} \text{pc}^{-2}$] versus $L_{12\mu\text{m}}$ [L_{\odot}] in the logarithmic space. All relations are characterized by the equation $y = kx + b$, along with the derived intrinsic scatter σ_{int} and the Spearman’s correlation coefficient r provided by *LinMix* fitting.

Only the low mass ($M_* \leq 10^{10} M_{\odot}$) galaxies show a weak dependence ($r = 0.5$) of $\Delta \log(L_{\text{CO}(1-0)})$ on integrated stellar mass, which are similar to the low mass SFGs where the presence of CO-dark molecular gas is possibly increasing (Kim et al. 2022). But this dependence on stellar mass can not fully explain the different slope between early-type and star-forming galaxies.

4. DISCUSSION

4.1. Physical Origin of the higher slope in ETGs

The CO–mid-IR correlation is often interpreted as reflecting the relationship between molecular gas as the fuel and the resulting star formation. However, ETGs are significantly fainter than SFGs in both 12 μm and CO bands. The steeper CO–mid-IR slope observed in ETGs suggests either less CO relative to mid-IR emission or, equivalently, more mid-IR emission per unit molecular gas. If SFRs were solely estimated from 12 μm emission, this would imply paradoxically shorter molecular depletion times in ETGs compared to SFGs, a conclusion that conflicts with observational evidence (e.g., Colombo et al. 2018).

These excess mid-IR emissions relative to CO likely originate from processes unrelated to recent star formation or its fuel (i.e., molecular gas traced by CO). Such contributions may include “cirrus” emission from dust heated by older stellar populations (Donoso et al. 2012; Villaume et al. 2015) and the widespread presence of PAHs in diverse astrophysical environments (Tielens 2008; Hudgins & Allamandola 2005).

There are two potential theoretical explanations for the steeper CO–mid-IR slope observed in ETGs. First, while

the deviations $\Delta \log(L_{\text{CO}})$ do not correlate with sSFR, numerous studies have highlighted the significant influence of older stars on mid-IR broadband photometry. The excitation of PAHs by older stars is particularly prominent in late-type flocculent spirals (Temi et al. 2009; Bendo et al. 2020). To address this, we applied a methodology similar to that in Davis et al. (2014) (Appendix A) to subtract the contribution of circumstellar dust around hot old stars from the 12 μm emission, recovering the correlation between 12 μm and CO (1-0) luminosities typical of star-forming galaxies. Additionally, the lack of dependence of these deviations on sSFR may arise from contamination in far-IR emission used to compute SFR, which can include contributions from mass-losing red giant stars and buoyantly transported or accreted dust (Temi et al. 2009), coupled with the fact that sSFR represents an integrated property rather than a local one.

The second potential interpretation is that the PAHs traces the interstellar medium (ISM) more directly (Li 2020), because the diffuse PAH emission typically encompasses, rather than residing within, the star-forming region containing ionized gas and hot dust (Watson et al. 2008). Notably, the PAH flux at the 11.3 μm band shows a strong enhancement in ETGs, which should be dominated by electronic collisions instead of stellar photons (Kaneda et al. 2008). As a result, PAHs in these elliptical galaxies can act as tracers for the gas present in these galaxies’ harsh environments as reviewed by Bolatto et al. (2013) and Saintonge & Catinella (2022). Moreover, the lack of CO emission that effectively means higher α_{CO} could also be explained if the fraction of molecular gas in a CO-dark phase or atomic hydrogen gas (Walterbos & Schwing 1987) is increased within regions with lower Σ_{H_2} .

In such areas, mid-IR such as PAH emission might still be visible, even though CO is very faint (Chastenot et al. 2019; Leroy et al. 2023a; Sandstrom et al. 2023; Whitcomb et al. 2023). And the dark-gas fraction is insensitive to radiation field but could be high as column densities become small (Wolfire et al. 2010). Then we do a simple and rough attempt in Appendix B, and discover the deviations could be significantly decreased, by adding a constant CO brightness density, averaging $2.8^{+0.8}_{-0.6}$ [K km s⁻¹] and $4.4^{+2.2}_{-1.4}$ [K km s⁻¹] for CO (1-0) and (2-1) respectively, which is assumed to correct the potential CO dark gas. These findings maybe hints of higher R_{21} (averaging 1.57) within the regions with lower Σ_{mol} , where the ratio covers a relatively wide range (Koda et al. 2020), or more CO (2-1) dark gas than CO (1-0) one.

We find that the CO deviation between ETGs and SFGs could diminish after applying corrections based on either of these two hypotheses. However, it's challenging to conclusively determine a preference. At the most basic level, we affirm that the ETGs resemble the CO non-detected regions in SFGs. Practically, we make a much more powerful attempt to assess the bias in molecular gas mass estimates from 12 μ m in ETGs, and provide a potential method to correct this bias.

5. SUMMARY

We conducted an initial investigation into the relationship between CO and *WISE* 12 μ m emission in early-type galaxies. Utilizing a sample of 352 nearby ETGs, we determined the correlations between CO and 12 μ m luminosities for both CO (1-0) and CO (2-1), and compared them to those from SFGs. To elucidate the differences, we then explored the deviations as functions of the host galaxy's properties and local molecular gas. Our main conclusions can be summarized as follows:

1. We confirm strong power law correlations also exist between L_{CO} and $L_{12\mu m}$ in early-type galaxies. Compared to the typical star-forming global (galaxy-wide) galaxies, both $L_{CO(1-0)}$ vs. $L_{12\mu m}$ and $L_{CO(2-1)}$ vs. $L_{12\mu m}$ relations in ETGs exhibit steeper slopes.
2. Based on these same detected ETGs, CO (1-0) and CO (2-1) display identical slopes in their CO versus 12 μ m relations. This indicate that R_{21} remains unchanged regardless of the mid-IR emission, which is notably different from the behavior observed in SFGs.
3. For these ETGs, we compute the L_{CO} deviations relative to the typical best-fitting relations with $L_{12\mu m}$ measured based on SFGs. These deviations, $\Delta \log(L_{CO(1-0)})$ and $\Delta \log(L_{CO(2-1)})$, show no dependence on galaxy-integrated properties color, sSFR, and morphology. Only ETGs with the low stellar masses are significantly below the typical $L_{CO(1-0)}$ vs. $L_{12\mu m}$ relation in SFGs.
4. The correlations between $L_{CO(1-0)}$ and $L_{12\mu m}$ in ETGs and SFGs can be brought into agreement by correcting estimated 12 μ m emission from circumstellar material around old stars in ETGs. We further found that the deviations in the L_{CO} strongly depend on molecular gas densities, essentially as evidence for a systematically different α_{CO} , which is consistent with a scenario that the mid-IR flux from atomic or CO-dark gas is increased relative to CO-bright gas in regions with lower Σ_{mol} . Subsequently, we discovered that such dependencies can be eliminated, by adding a constant additional CO brightness density ($2.8^{+0.8}_{-0.6}$ [K km s⁻¹] and $4.4^{+2.2}_{-1.4}$ [K km s⁻¹] to CO (1-0) and (2-1) luminosity respectively), which may correspond to gas not traceable by CO but potentially linked to mid-infrared emission.

Given the small scatter even in these gas-poor ETGs, we contend that applying the (corrected) L_{CO} vs. $L_{12\mu m}$ relations to estimate the molecular gas content would offer significant potential advantages. Such application could greatly enhance our analytical capabilities across all types of nearby galaxy, especially considering the rare and valuable detection of molecular gas in ETGs.

ACKNOWLEDGEMENTS

This work is supported by the International Centre of Supernovae, Yunnan Key Laboratory (Nos. 202302AN360001 and 202302AN36000103), Shandong Provincial Natural Science Foundation (ZR2023MA036) and the National Science Foundation of China (grant Nos.12033004, 12233005, 11861131007, 11803090, 12303015 and 12003070). YG receives funding from Scientific Research Fund of Dezhou University (3012304024) and Shandong Provincial Natural Science Foundation (ZR2024QA212). EW thanks support of the Start-up Fund of the University of Science and Technology of China (No. KY2030000200). FHL acknowledges support from the ESO Studentship Programme and the Scatcherd European Scholarship of the University of Oxford. QJ receives Research Funding of Wuhan Polytechnic University NO. 2022RZ035. D.D.S. acknowledges the National Science Foundation of Jiangsu Province (BK20231106). We are deeply grateful to Prof. Yu Gao for his invaluable guidance and suggestions about the sample and data. And we extend our heartfelt thanks to Prof. Cheng Li and Mr. Tao Jing for their exceptional technical assistance throughout the data analysis process.

Funding for the NASA-Sloan Atlas has been provided by the NASA Astrophysics Data Analysis Program (08-ADP08-0072) and the NSF (AST-1211644).

Funding for SDSS-III has been provided by the Alfred P. Sloan Foundation, the Participating Institutions, the National

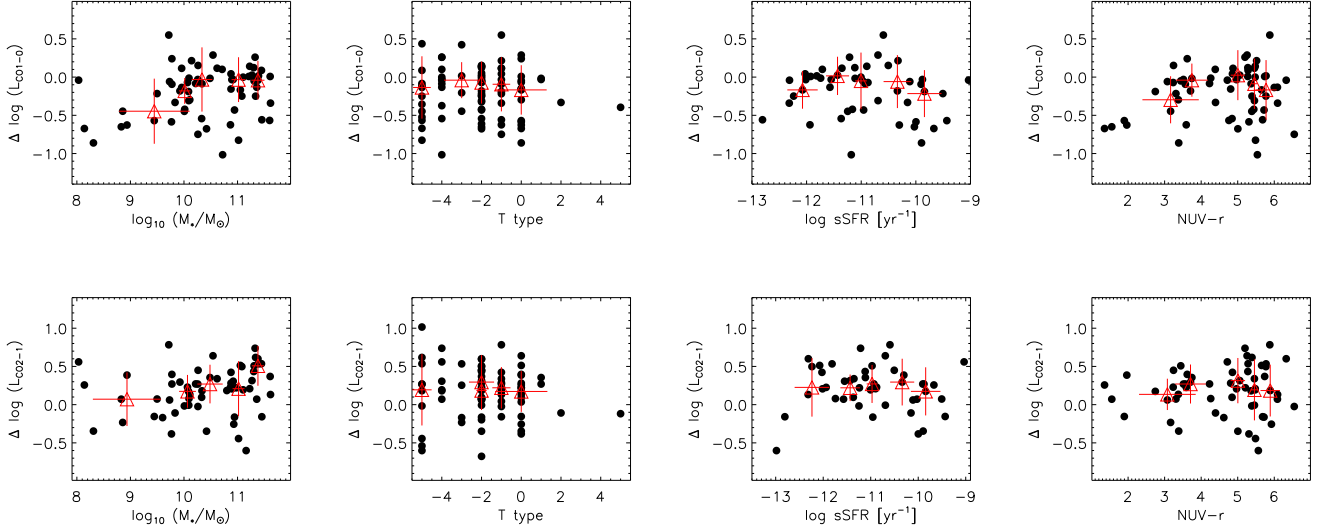


Figure 3. The scaling of $\Delta \log(L_{\text{CO}})$, calculated using Equations 5 and representing the deviation from typical star-forming global $L_{\text{CO}}-L_{12\mu\text{m}}$ relations (Gao et al. 2019), is plotted against the basic properties of integrated galaxies. These properties include stellar mass M_* , T type, sSFR and NUV- r color arranged from left to right. The plots show CO (1-0) in the top panels and CO (2-1) in the bottom panels. Large red triangles with error bars indicate the median and scatter for galaxies in 5 sub-samples from left to right.

Science Foundation, and the U.S. Department of Energy. The SDSS-III web site is <http://www.sdss3.org>.

SDSS-III is managed by the Astrophysical Research Consortium for the Participating Institutions of the SDSS-III Collaboration including the University of Arizona, the Brazilian Participation Group, Brookhaven National Laboratory, University of Cambridge, University of Florida, the French Participation Group, the German Participation Group, the Instituto de Astrofísica de Canarias, the Michigan State/Notre Dame/JINA Participation Group, Johns Hopkins University, Lawrence Berkeley National Laboratory, Max Planck Insti-

tute for Astrophysics, New Mexico State University, New York University, Ohio State University, Pennsylvania State University, University of Portsmouth, Princeton University, the Spanish Participation Group, University of Tokyo, University of Utah, Vanderbilt University, University of Virginia, University of Washington, and Yale University.

Software: SExtractor (Bertin & Arnouts 1996), LinMix (Kelly 2007), IDL Astronomy user’s library (Landsman 1995).

APPENDIX

A. THE POSSIBLE OLD STAR EMISSION IN WISE 12 μm BAND

In this section, we aim to correct the correlation between CO (1-0) and 12 μm luminosity in ETGs, by correcting the emission from old stars following the methodology used by Davis et al. (2014).

As shown in Figure 4, our sample of 210 CO non-detected galaxies (represented by open black circles) shows a clear correlation $r = 0.68 \pm 0.04$ between $L_{12\mu\text{m}}$ and M_* (from NSA catalog), despite a significant scatter of approximately 0.39 dex. The 62 ETGs with detected CO emissions (after matching with NSA) do not display a clear correlation and mostly lie above the average position of the CO non-detections at a given stellar mass, which maybe hint that the excess of their 12 μm emission is related to star formation. We perform a fit to roughly determine the mean amount of 12 μm emission caused by old stellar populations at each stellar mass. After subtracting the contributions from these older stars, 52 CO (1-0) detections and 107 non-detections have $L_{12\mu\text{m}}$ great than 0. Remarkably, the correlation between corrected 12 μm and CO (1-0) luminosity is closely mirrors that in SFGs⁵, as shown in Figure 5. This preliminary but convincing test suggests that the older stellar populations significantly

⁵ In SFGs, while more-evolved stellar populations can also contribute to the heating of PAH molecules (Ronayne et al. 2024), their contribution to the 12 μm emission is minimal, as shown by Hunt et al. (2019). For instance, the median fraction of this contribution is only about 7% in the xCOLD GASS sample.

contribute the steeper slope we observe. Future studies will provide more detailed analyses and explore the relation for CO (2-1) in subsequent papers.

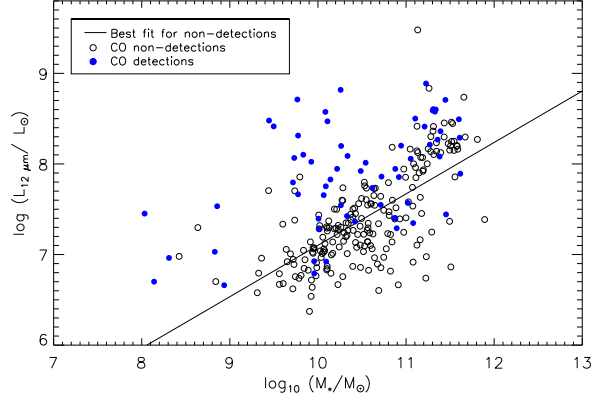


Figure 4. The *WISE* 12 μm luminosity within CO(1-0) beam is plotted as a function of stellar mass. Blue circles are ETGs with CO detection, while open circles represent those without detected molecular gas. The best fit of these non-detections is shown as a black solid line.

B. THE POSSIBLE COMPONENTS FROM CO-DARK GAS

We plot the correlation between $\Delta \log(L_{\text{CO}})$ and molecular gas surface density (Σ_{H_2}) in Figure 6, for the CO detected ETGs. The Σ_{H_2} is converted using galactic $\alpha_{\text{CO}} = 3.2 \text{ M}_\odot (\text{K km s}^{-1} \text{ pc}^2)^{-1}$ and $R21 = 0.7$ from CO (1-0) and CO (2-1) brightness density, which is roughly calculated based on the beam size of telescope for the ETGs observed with single dish, simply assuming the gas disc fills the beam based on some sizes listed in (Davis et al. 2013).

The dependence is quite strong for both $\Delta \log(L_{\text{CO}(1-0)})$ and $\Delta \log(L_{\text{CO}(2-1)})$ in ETGs, with $r = 0.67 \pm 0.08$ (0.55 ± 0.10 after subtracting the old stars' emission such in Figure 5) and 0.68 ± 0.08 respectively, which is like and even more significant than the correlations observed in regions with very low molecular gas mass surface density in SFGs, as discussed in Gao et al. (2022).

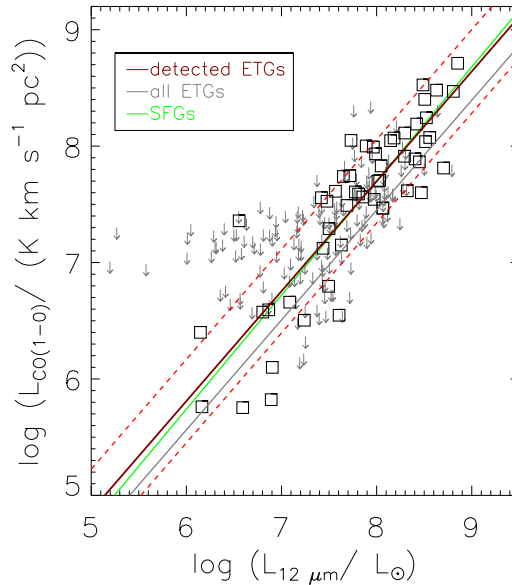


Figure 5. Same as the left panel of Figure 2, but based on the corrected 12 μm luminosity after subtracting the estimated old stars' emission.

The dependence on CO brightness instead of 12 μm brightness further strengthens our suspicion that the systematic higher α_{CO} is due to the underlying CO-dark gas.

We can compute the average contribution, considering a toy assumption that these CO-dark components are statistically expected to be spatially randomly distributed, which is $2.8^{+0.8}_{-0.8}$ [K km s^{-1}] ($2.2^{+1.2}_{-0.8}$ [K km s^{-1}] for the one after subtracting the old stars' emission in Appendix A) and $4.4^{+2.2}_{-1.4}$ [K km s^{-1}] for CO (1-0) and (2-1) brightness density, respectively. These values maybe unimportant in SFGs, so ETGs yield a significant chance to extract these additional CO-dark components. Besides being interpreted as a potential higher R_{21} , the higher average additional CO (2-1) background density may also suggest that the fraction of dark gas can't be traced by CO (2-1) exceed that untraceable by CO (1-0), as illustrated in the Figure 14 of [Gong et al. \(2020\)](#). After applying these constant brightness density correction to the CO (1-0) and CO (2-1) luminosity, the distributions of $\Delta \log(L_{\text{CO}})$ noticeably narrow, and the dependencies on Σ_{H_2} are almost eliminated, while the scatter in the correlations remains essentially unchanged.

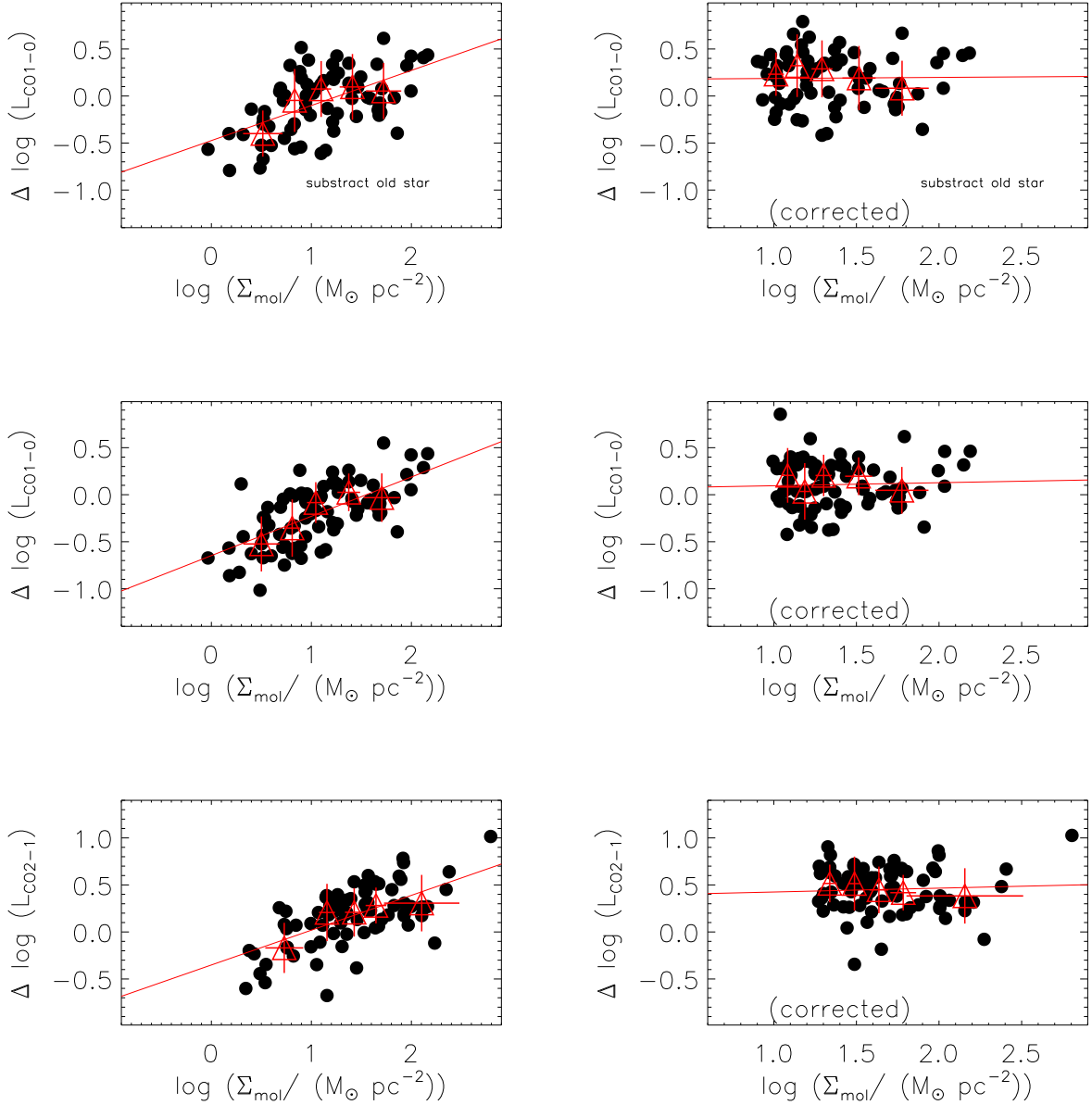


Figure 6. The left panels demonstrate the dependence of the CO luminosity deviations on molecular gas mass surface densities (Σ_{mol}), which are computed based on CO (1-0) or CO (2-1) surface brightness using the galactic conversion factor $\alpha_{\text{CO}} = 3.2 M_{\odot}(\text{K km s}^{-1} \text{pc}^2)^{-1}$ and $R_{21} = 0.7$ (Leroy et al. 2013). And the top panel is based on the correlation between CO (1-0) and $12 \mu\text{m}$ luminosities, after subtracting old stars' emission as shown in Figure 5. The right panels display the corrected correlations, by adding a constant CO brightness density, which is for CO dark gas, in both x- and y- axes (from top to bottom: $2.2 [\text{K km s}^{-1}]$ and $2.8 [\text{K km s}^{-1}]$ for CO (1-0), and $4.4 [\text{K km s}^{-1}]$ for CO (2-1)).

Table 2. CO and MIR properties of the ETG sample objects.

Galaxy	D_L	$L_{\text{CO}(1-0)}$	$L_{12\mu\text{m}(1-0)}$	$\text{ref}_{(1-0)}$	$\text{Beam}_{(1-0)}$	$L_{\text{CO}(2-1)}$	$L_{12\mu\text{m}(2-1)}$	$\text{ref}_{(2-1)}$	$\text{Beam}_{(2-1)}$
(1)	(Mpc)	(10^6 [K km s $^{-1}$ pc $^{-2}$])	(10^7 L $_{\odot}$)	(5)	(arcsec)	(10^6 [K km s $^{-1}$ pc $^{-2}$])	(10^7 L $_{\odot}$)	(9)	(arcsec)
(1)	(2)	(3)	(4)	(5)	(6)	(7)	(8)	(9)	(10)
IC0310	77.5	175.1 \pm 21.3	40.28 \pm 2.16	4	22	129.9 \pm 5.9	16.64 \pm 1.12	4	11
IC0560	27.2	< 14.92	1.957 \pm 0.134	1	22	< 8.148	0.7445 \pm 0.0725	1	11
IC0598	35.3	< 33.10	2.022 \pm 0.164	1	22	< 9.505	0.8164 \pm 0.0955	1	11
IC0676	24.6	81.89 \pm 3.02	20.56 \pm 0.91	1	22	29.29 \pm 0.60	7.126 \pm 0.347	1	11
IC0719	29.4	34.88 \pm 3.63	10.56 \pm 0.51	1	22	14.56 \pm 0.78	3.604 \pm 0.216	1	11
IC0782	36.3	< 26.27	0.5824 \pm 0.0849	1	22	< 6.376	0.2081 \pm 0.0487	1	11
IC1024	24.2	77.73 \pm 2.91	25.99 \pm 1.13	1	22	26.60 \pm 0.68	9.820 \pm 0.458	1	11
IC3631	42.0	< 27.48	1.139 \pm 0.139	1	22	< 6.023	0.4463 \pm 0.0828	1	11
NGC0057	76.3	< 50.09	16.74 \pm 1.12	4	22	< 32.25	6.155 \pm 0.591	4	11
NGC0227	75.9	< 42.06	13.97 \pm 0.98	4	22	< 23.28	5.473 \pm 0.546	4	11
NGC0315	70.3	< 224.2	54.53 \pm 2.68	4	22				
NGC0383	71.3	335.6 \pm 47.9	37.79 \pm 1.98	4	22	207.7 \pm 16.7	15.78 \pm 1.02	4	11
NGC0448	29.5	< 17.45	2.086 \pm 0.148	1	22	< 4.995	0.7672 \pm 0.0791	1	11
NGC0467	75.8	98.14 \pm 17.77	19.48 \pm 1.24	4	22	39.31 \pm 8.35	7.571 \pm 0.661	4	11
NGC0474	31.6	< 14.53	2.470 \pm 0.173	2	22	< 5.085	0.8887 \pm 0.0911	2	11
NGC0499	69.8	< 44.93	14.59 \pm 0.96	4	22	< 19.40	5.456 \pm 0.508	4	11
NGC0502	35.9	< 23.97	2.055 \pm 0.168	1	22	< 5.449	0.7846 \pm 0.0948	1	11
NGC0507	69.8	< 60.79	14.11 \pm 0.94	4	22	< 37.48	5.159 \pm 0.491	4	11
NGC0509	32.3	5.785 \pm 1.880	0.8436 \pm 0.0912	1	22	< 2.501	0.3277 \pm 0.0539	1	11
NGC0516	34.7	< 21.20	0.7449 \pm 0.0911	1	22	< 7.733	0.2622 \pm 0.0516	1	11
NGC0524	23.3	17.94 \pm 2.20	7.805 \pm 0.371	1	22	7.618 \pm 0.653	2.820 \pm 0.160	1	11
NGC0525	30.7	< 18.08	0.6230 \pm 0.0739	1	22	< 5.026	0.2320 \pm 0.0430	1	11
NGC0533	77.9	< 74.56	14.54 \pm 1.03	4	22	< 43.11	5.175 \pm 0.539	4	11
NGC0547	74.0	< 65.81	14.70 \pm 1.00	4	22	< 35.40	5.658 \pm 0.545	4	11
NGC0661	30.6	< 17.90	2.324 \pm 0.162	1	22	< 5.823	0.8768 \pm 0.0878	1	11
NGC0665	74.6	252.2 \pm 18.6	38.92 \pm 2.07	4	22	95.94 \pm 6.30	14.79 \pm 1.01	4	11
NGC0680	37.5	< 23.78	5.512 \pm 0.335	1	22	< 7.437	2.064 \pm 0.173	1	11
NGC0708	69.0	101.8 \pm 17.2	11.20 \pm 0.80	4	22				
NGC0741	73.9	< 57.90	15.96 \pm 1.06	4	22	< 37.19	5.572 \pm 0.539	4	11
NGC0770	36.7	< 24.97	1.212 \pm 0.124	1	22	< 5.988	0.4982 \pm 0.0755	1	11
NGC0821	23.4	< 10.53	2.643 \pm 0.152	1	22	< 1.957	0.9685 \pm 0.0757	1	11
NGC0890	55.6	< 43.99	12.07 \pm 0.74	4	22	< 29.40	4.424 \pm 0.374	4	11
NGC0910	79.8	< 34.62	11.64 \pm 0.90	4	22	< 24.35	4.238 \pm 0.492	4	11
NGC0936	22.4	< 9.448	3.501 \pm 0.186	1	22	< 2.012	1.210 \pm 0.085	1	11
NGC0997	90.4	302.7 \pm 22.5	50.98 \pm 2.78	4	22	171.5 \pm 8.5	20.20 \pm 1.41	4	11
NGC1023	10.3	< 1.535	1.552 \pm 0.074	2	22	< 0.5374	0.5421 \pm 0.0308	2	11
NGC1060	67.4	< 20.04	18.64 \pm 1.12	4	22	< 26.93	6.885 \pm 0.570	4	11
NGC1106	63.3	140.0 \pm 6.6	119.8 \pm 5.3	3	22	28.00 \pm 3.00	48.72 \pm 2.36	3	11
NGC1121	35.3	< 20.50	1.461 \pm 0.135	1	22	< 6.264	0.5991 \pm 0.0808	1	11
NGC1129	73.9	< 224.2	12.71 \pm 0.91	4	22				
NGC1132	97.6	< 82.38	15.85 \pm 1.27	4	22	< 35.31	5.447 \pm 0.675	4	11
NGC1167	70.2	67.59 \pm 5.73	18.54 \pm 1.14	4	22	16.90 \pm 2.86	6.555 \pm 0.570	4	11
NGC1222	33.3	223.7 \pm 6.8	116.5 \pm 4.9	1	22	92.68 \pm 1.80	45.04 \pm 1.97	1	11
NGC1248	30.4	< 15.42	1.607 \pm 0.127	1	22	< 3.773	0.5977 \pm 0.0704	1	11
NGC1266	29.9	363.3 \pm 11.1	27.08 \pm 1.20	1	22	271.2 \pm 2.4	11.28 \pm 0.54	1	11
NGC1289	38.4	< 24.42	3.155 \pm 0.232	1	22	< 7.349	1.193 \pm 0.127	1	11
NGC128-HI	58.5	35.95 \pm 3.78	15.25 \pm 0.90	3	22	4.000 \pm 1.000	3.127 \pm 0.318	3	11
NGC1453	53.5	< 28.33	13.03 \pm 0.76	3	22	< 5.106	5.289 \pm 0.423	4	11
NGC1497	87.8	209.6 \pm 25.8	69.77 \pm 3.54	4	22	135.5 \pm 9.9	29.28 \pm 1.80	4	11
NGC1550	52.1	< 16.67	7.896 \pm 0.524	3	22	< 6.667	3.033 \pm 0.283	3	11
NGC1573	65.0	< 38.63	12.02 \pm 0.80	4	22	< 20.20	4.288 \pm 0.416	4	11
NGC1600	63.8	< 89.25	8.992 \pm 0.651	11	15				
NGC1665	37.5	< 28.52	1.664 \pm 0.153	1	22	< 8.050	0.5989 \pm 0.0854	1	11
NGC1684	63.5	266.9 \pm 14.3	39.97 \pm 2.00	4	22	148.6 \pm 4.0	15.73 \pm 0.96	4	11
NGC1700	54.4	< 70.89	31.62 \pm 1.56	11	44	< 13.09	16.36 \pm 0.91	11	23
NGC2256	79.4	< 66.35	12.47 \pm 0.94	4	22	< 36.02	4.213 \pm 0.489	4	11
NGC2258	59.0	< 51.22	12.07 \pm 0.76	4	22	< 15.44	4.258 \pm 0.383	4	11
NGC2274	73.8	< 41.78	14.78 \pm 1.00	4	22	< 24.13	5.477 \pm 0.534	4	11
NGC2320	89.4	1099.9 \pm 157.1	86.46 \pm 4.32	13	entire				

Galaxy	D_L	$L_{CO(1-0)}$	$L_{12\mu m(1-0)}$	ref ₍₁₋₀₎	Beam ₍₁₋₀₎	$L_{CO(2-1)}$	$L_{12\mu m(2-1)}$	ref ₍₂₋₁₎	Beam ₍₂₋₁₎
(1)	(Mpc)	(10^6 [K km s ⁻¹ pc ⁻²])	($10^7 L_\odot$)	(5)	(arcsec)	(10^6 [K km s ⁻¹ pc ⁻²])	($10^7 L_\odot$)	(9)	(arcsec)
(2)	(3)	(4)	(7)	(8)	(10)				
NGC2418	74.1	< 166.2	23.05 ± 1.38	11	33				
NGC2481	32.0	< 19.40	3.516 ± 0.222	1	22	< 7.320	1.427 ± 0.122	1	11
NGC2513	70.8	< 36.09	13.81 ± 0.93	4	22	< 23.77	5.286 ± 0.506	4	11
NGC252	71.7	129.6 ± 16.1	25.84 ± 1.48	3	22	< 18.33	7.466 ± 0.627	3	11
NGC2549	16.8	< 6.196	1.628 ± 0.090	2	22	< 2.161	0.6094 ± 0.0443	2	11
NGC2563	64.4	< 33.33	9.133 ± 0.664	3	22	< 10.00	3.419 ± 0.362	3	11
NGC2577	30.8	< 16.21	3.644 ± 0.223	1	22	< 5.196	1.460 ± 0.120	1	11
NGC2592	25.0	< 11.08	1.736 ± 0.117	1	22	< 3.160	0.6774 ± 0.0639	1	11
NGC2594	35.1	< 21.62	1.103 ± 0.114	1	22	< 4.618	0.4451 ± 0.0684	1	11
NGC2672	61.5	< 42.74	11.81 ± 0.77	4	22	< 32.56	4.187 ± 0.392	4	11
NGC2679	30.6	< 20.71	1.202 ± 0.108	2	22	< 4.768	0.4849 ± 0.0634	2	11
NGC2685	16.7	3.754 ± 0.729	1.912 ± 0.102	1	22	< 1.722	0.6218 ± 0.0448	1	11
NGC2693	74.4	< 47.25	26.06 ± 1.51	4	22	< 31.26	10.31 ± 0.79	4	11
NGC2695	23.2	< 16.00	1.522 ± 0.102	2	22	< 5.489	0.5785 ± 0.0549	2	11
NGC2698	27.1	< 10.12	3.188 ± 0.189	1	22				
NGC2699	23.2	< 7.841	1.372 ± 0.095	2	22	< 2.744	0.5255 ± 0.0518	2	11
NGC2764	39.6	295.3 ± 10.6	65.73 ± 2.86	1	22	111.2 ± 3.9	23.72 ± 1.12	1	11
NGC2768	21.5	8.045 ± 1.502	3.560 ± 0.186	2	22	3.352 ± 0.630	1.213 ± 0.083	2	11
NGC2778	22.3	< 9.538	0.7848 ± 0.0644	1	22	< 2.977	0.2988 ± 0.0363	1	11
NGC2783	101.4	< 58.66	19.84 ± 1.51	4	22	< 19.90	7.273 ± 0.824	4	11
NGC2824	40.7	85.88 ± 6.43	16.33 ± 0.82	1	22	29.72 ± 2.54	6.585 ± 0.399	1	11
NGC2832	105.2	< 97.70	28.33 ± 1.96	4	22	< 61.84	10.11 ± 1.03	4	11
NGC2852	28.5	< 15.34	1.033 ± 0.092	1	22	< 4.237	0.4327 ± 0.0555	1	11
NGC2859	27.0	< 13.09	4.478 ± 0.245	1	22	< 3.856	1.593 ± 0.116	1	11
NGC2880	21.3	< 8.860	1.374 ± 0.090	1	22	< 3.369	0.5065 ± 0.0472	1	11
NGC2892	101.1	< 241.6	17.74 ± 1.40	4	22				
NGC2911	45.8	54.87 ± 6.62	12.07 ± 0.67	3	22	38.00 ± 3.00	4.540 ± 0.331	3	11
NGC2950	14.5	< 4.240	1.667 ± 0.087	1	22	< 1.421	0.6307 ± 0.0414	1	11
NGC2962	34.0	< 22.57	4.038 ± 0.254	1	22	< 11.96	1.533 ± 0.134	1	11
NGC2974	24.3	< 17.53	6.733 ± 0.330	2	22	< 6.016	2.564 ± 0.152	2	11
NGC3032	21.7	50.81 ± 1.64	11.65 ± 0.52	2	22	10.79 ± 0.31	4.471 ± 0.225	2	11
NGC3073	32.8	6.253 ± 1.038	3.412 ± 0.220	7	22	1.407 ± 0.259	1.312 ± 0.118	7	11
NGC3098	23.0	< 9.377	1.318 ± 0.092	1	22	< 2.621	0.4837 ± 0.0491	1	11
NGC3156	15.1	4.263 ± 0.986	0.8359 ± 0.0519	2	22	0.5995 ± 0.1532	0.3185 ± 0.0272	2	11
NGC3158	103.4	< 78.77	28.93 ± 1.96	4	22	< 50.74	10.82 ± 1.05	4	11
NGC3182	34.0	40.41 ± 4.65	8.347 ± 0.441	1	22	13.99 ± 0.89	3.074 ± 0.209	1	11
NGC3193	33.1	< 25.79	5.455 ± 0.313	1	22	< 5.014	2.017 ± 0.156	1	11
NGC3226	22.9	< 8.260	3.938 ± 0.207	1	22	< 2.240	1.503 ± 0.100	1	11
NGC3230	40.8	< 31.73	5.077 ± 0.333	1	22	< 13.81	1.875 ± 0.175	1	11
NGC3245	20.3	3.525 ± 1.092	7.246 ± 0.336	1	22	< 1.533	2.999 ± 0.158	1	11
NGC3248	24.6	< 11.29	0.9905 ± 0.0800	1	22	< 4.247	0.3714 ± 0.0447	1	11
NGC3301	22.8	< 9.094	3.175 ± 0.174	1	22	< 2.047	1.213 ± 0.086	1	11
NGC3325	79.7	< 56.67	7.974 ± 0.718	3	22	< 20.00	2.956 ± 0.405	3	11
NGC3377	10.7	< 2.514	0.7207 ± 0.0391	2	22	< 0.8767	0.2503 ± 0.0181	2	11
NGC3379	10.7	< 1.654	1.713 ± 0.081	2	22	< 0.5790	0.5947 ± 0.0336	2	11
NGC3384	10.7	< 3.375	1.477 ± 0.071	2	22	< 1.158	0.5449 ± 0.0315	2	11
NGC3400	24.7	< 13.62	0.5704 ± 0.0579	1	22	< 2.739	0.2019 ± 0.0324	1	11
NGC3412	11.0	< 2.904	0.7157 ± 0.0394	1	22	< 0.4729	0.2637 ± 0.0192	1	11
NGC3414	20.1	< 3.065	2.698 ± 0.145	2	22	< 1.061	0.9522 ± 0.0675	2	11
NGC3457	20.1	< 7.115	0.8763 ± 0.0641	1	22	< 1.796	0.3275 ± 0.0349	1	11
NGC3458	30.9	< 17.04	2.097 ± 0.152	1	22	< 3.094	0.8116 ± 0.0847	1	11
NGC3489	10.7	2.514 ± 0.397	2.312 ± 0.106	2	22	0.6286 ± 0.1092	0.8057 ± 0.0427	2	11
NGC3499	26.4	< 13.16	2.397 ± 0.151	1	22	< 2.522	0.9017 ± 0.0792	1	11
NGC3522	25.5	< 6.047	0.4683 ± 0.0536	10	22	< 2.645	0.1943 ± 0.0328	10	11
NGC3530	31.2	< 19.29		1	22	< 4.314		1	11
NGC3595	34.7	< 21.76	2.217 ± 0.171	1	22	< 4.111	0.8384 ± 0.0954	1	11
NGC3599	19.8	< 5.035	2.165 ± 0.121	1	22	1.093 ± 0.208	0.9166 ± 0.0651	1	11
NGC3605	20.1	< 9.627	0.6142 ± 0.0512	7	22	< 2.113	0.2296 ± 0.0287	7	11
NGC3607	22.2	50.07 ± 5.56	12.25 ± 0.55	6	22	14.11 ± 0.80	4.438 ± 0.225	6	11
NGC3608	15.6	< 5.347	1.077 ± 0.063	2	22	< 1.231	0.3883 ± 0.0315	2	11

Galaxy	D_L	$L_{\text{CO}(1-0)}$	$L_{12\mu\text{m}(1-0)}$	$\text{ref}_{(1-0)}$	$\text{Beam}_{(1-0)}$	$L_{\text{CO}(2-1)}$	$L_{12\mu\text{m}(2-1)}$	$\text{ref}_{(2-1)}$	$\text{Beam}_{(2-1)}$
(1)	(Mpc)	(10^6 [K km s $^{-1}$ pc $^{-2}$])	($10^7 L_\odot$)	(5)	(arcsec)	(10^6 [K km s $^{-1}$ pc $^{-2}$])	($10^7 L_\odot$)	(9)	(arcsec)
(2)	(3)	(4)	(6)	(7)	(8)	(10)			
NGC3610	20.8	< 8.046	3.428 \pm 0.178	1	22	< 2.954	1.303 \pm 0.085	1	11
NGC3613	28.3	< 14.38	3.815 \pm 0.221	1	22	< 3.410	1.354 \pm 0.108	1	11
NGC3619	26.8	36.05 \pm 4.26	5.440 \pm 0.285	1	22	7.944 \pm 1.413	1.906 \pm 0.130	1	11
NGC3626	19.5	30.93 \pm 2.91	8.815 \pm 0.399	1	22	12.47 \pm 0.63	3.226 \pm 0.165	1	11
NGC3630	25.0	< 12.71	1.926 \pm 0.126	1	22	< 3.133	0.7412 \pm 0.0675	1	11
NGC3640	26.3	< 12.30	4.288 \pm 0.234	1	22	< 2.663	1.472 \pm 0.108	1	11
NGC3641	25.9	< 14.54	0.6008 \pm 0.0623	1	22	< 3.684	0.2435 \pm 0.0374	1	11
NGC3648	31.9	< 18.87	1.888 \pm 0.145	1	22	< 5.500	0.7116 \pm 0.0807	1	11
NGC3658	32.7	< 21.07	3.628 \pm 0.230	1	22	< 5.593	1.474 \pm 0.126	1	11
NGC3665	33.1	154.8 \pm 8.4	31.69 \pm 1.41	1	22	45.36 \pm 2.66	12.37 \pm 0.61	1	11
NGC3674	33.4	< 19.32	2.236 \pm 0.168	1	22	< 4.182	0.8509 \pm 0.0929	1	11
NGC3694	35.2	< 25.92	7.179 \pm 0.397	1	22	< 7.831	2.979 \pm 0.210	1	11
NGC3757	22.6	< 9.677	0.8331 \pm 0.0673	1	22	< 1.840	0.3324 \pm 0.0389	1	11
NGC3796	22.7	< 10.18	0.8843 \pm 0.0701	1	22	< 2.022	0.3586 \pm 0.0408	1	11
NGC3805	99.4	< 69.28	68.44 \pm 3.65	12	31				
NGC3816	99.4	< 55.04	13.36 \pm 1.17	4	22	< 25.50	4.847 \pm 0.647	4	11
NGC3838	23.5	< 10.85	1.245 \pm 0.090	1	22	< 2.183	0.4923 \pm 0.0504	1	11
NGC3842	99.4	< 49.05	25.91 \pm 1.79	12	31				
NGC3862	99.4	41.38 \pm 3.48	31.14 \pm 2.02	4	22				
NGC3941	11.9	< 2.469	1.377 \pm 0.069	1	22	< 0.5597	0.5017 \pm 0.0313	1	11
NGC3945	23.2	< 10.01	4.156 \pm 0.217	1	22	< 1.885	1.487 \pm 0.100	1	11
NGC3998	13.7	< 3.687	5.358 \pm 0.239	1	22	< 0.7363	2.203 \pm 0.107	1	11
NGC4008	54.0	< 26.67	7.128 \pm 0.500	3	22	< 10.00	2.594 \pm 0.266	3	11
NGC4026	13.2	< 3.139	1.260 \pm 0.067	1	22	< 0.5266	0.4648 \pm 0.0316	1	11
NGC4036	24.6	< 17.30	6.213 \pm 0.309	1	22	6.464 \pm 0.568	2.181 \pm 0.136	1	11
NGC4055	107.2	109.3 \pm 15.6	39.84 \pm 2.51	4	22	432.1 \pm 8.6	39.17 \pm 1.96	14	entire
NGC4073	91.5	< 85.19	20.04 \pm 1.42	4	22	< 34.89	7.077 \pm 0.743	4	11
NGC4078	38.1	< 30.37	3.156 \pm 0.230	1	22	< 12.09	1.221 \pm 0.128	1	11
NGC410	76.7	< 41.67	19.80 \pm 1.26	3	22	< 13.33	7.228 \pm 0.648	3	11
NGC4111	14.6	3.196 \pm 0.719	3.499 \pm 0.164	6	22	2.354 \pm 0.217	1.354 \pm 0.073	6	11
NGC4119	16.5	14.36 \pm 1.01	2.527 \pm 0.128	1	22	4.578 \pm 0.344	0.9752 \pm 0.0608	1	11
NGC4143	15.5	< 5.013	2.409 \pm 0.120	6	22	< 1162.4	0.9318 \pm 0.0568	6	11
NGC4150	13.7	13.27 \pm 1.07	2.831 \pm 0.134	2	22	7.179 \pm 0.256	1.102 \pm 0.061	2	11
NGC4168	30.9	< 17.42	2.542 \pm 0.174	1	22	< 7.131	0.8858 \pm 0.0892	1	11
NGC4169	56.7	29.33 \pm 6.62	15.92 \pm 0.91	3	22	9.000 \pm 2.000	6.045 \pm 0.462	3	11
NGC4179	16.5	< 6.060	1.674 \pm 0.091	1	22	< 1.535	0.6193 \pm 0.0444	1	11
NGC4191	39.2	< 27.69	3.262 \pm 0.240	1	22	< 5.872	1.098 \pm 0.124	1	11
NGC4203	14.7	4.722 \pm 0.527	3.215 \pm 0.152	6	22	< 1045.5	1.227 \pm 0.068	6	11
NGC4215	31.5	< 21.34	2.503 \pm 0.174	1	22	< 5.551	0.9534 \pm 0.0947	1	11
NGC4233	33.9	< 24.51	5.407 \pm 0.314	1	22	< 12.26	2.129 \pm 0.164	1	11
NGC4249	38.7	< 29.60	0.7002 \pm 0.0980	1	22	< 6.115	0.2390 \pm 0.0551	1	11
NGC4251	19.1	< 4.134	2.589 \pm 0.137	6	22	< 2.210	0.9230 \pm 0.0638	6	11
NGC4255	31.2	< 19.24	1.955 \pm 0.147	1	22	< 3.564	0.7618 \pm 0.0826	1	11
NGC4259	37.2	< 29.60	0.7165 \pm 0.0958	1	22	< 11.84	0.2950 \pm 0.0589	1	11
NGC4261	31.6	< 14.53	10.04 \pm 0.50	2	22	< 5.085	3.794 \pm 0.233	2	11
NGC4262	16.3	< 3.856	1.246 \pm 0.072	2	22	< 1.349	0.4864 \pm 0.0376	2	11
NGC4264	37.5	< 27.95	1.742 \pm 0.157	1	22	< 5.558	0.6213 \pm 0.0869	1	11
NGC4267	15.8	< 4.556	1.273 \pm 0.073	1	22	< 1.567	0.4808 \pm 0.0365	1	11
NGC4268	31.7	< 21.73	1.375 \pm 0.119	1	22	< 5.066	0.5110 \pm 0.0671	1	11
NGC4270	16.3	< 3.856	0.5491 \pm 0.0409	2	22	< 0.6940	0.1997 \pm 0.0220	2	11
NGC4278	13.7	4.568 \pm 0.892	2.486 \pm 0.119	2	22	1.523 \pm 0.326	0.9002 \pm 0.0519	2	11
NGC4281	24.4	< 23.98	7.189 \pm 0.349	1	22	< 5.208	2.783 \pm 0.162	1	11
NGC4283	15.3	2.394 \pm 0.571	0.6175 \pm 0.0423	7	22	< 0.8843	0.2320 \pm 0.0227	7	11
NGC4324	16.5	9.351 \pm 1.057	1.949 \pm 0.103	1	22	1.564 \pm 0.229	0.5798 \pm 0.0425	1	11
NGC4339	16.0	< 4.538	0.6703 \pm 0.0462	1	22	< 1.064	0.2366 \pm 0.0240	1	11
NGC4340	18.4	< 6.867	1.032 \pm 0.068	1	22	< 1.825	0.3816 \pm 0.0355	1	11
NGC4342	16.5	< 5.475	0.9109 \pm 0.0580	1	22	< 1.175	0.3725 \pm 0.0321	1	11
NGC4346	13.9	< 4.200	0.9281 \pm 0.0536	1	22	< 0.8646	0.3507 \pm 0.0272	1	11
NGC4350	15.4	< 4.852	2.190 \pm 0.111	1	22	< 1.203	0.8551 \pm 0.0532	1	11
NGC4365	17.9	< 7.116	2.880 \pm 0.146	2	22	< 1.639	0.9923 \pm 0.0646	2	11

Galaxy	D_L	$L_{CO(1-0)}$	$L_{12\mu m(1-0)}$	ref ₍₁₋₀₎	Beam ₍₁₋₀₎	$L_{CO(2-1)}$	$L_{12\mu m(2-1)}$	ref ₍₂₋₁₎	Beam ₍₂₋₁₎
(1)	(Mpc)	(10^6 [K km s ⁻¹ pc ⁻²])	($10^7 L_\odot$)	(5)	(arcsec)	(10^6 [K km s ⁻¹ pc ⁻²])	($10^7 L_\odot$)	(9)	(arcsec)
(2)	(3)	(4)	(6)	(7)	(8)	(10)			
NGC4371	17.0	< 6.215	1.403 ± 0.081	1	22	< 2.662	0.4916 ± 0.0390	1	11
NGC4374	16.3	< 3.856	4.358 ± 0.204	2	22	< 1.349	1.530 ± 0.085	2	11
NGC4377	17.8	< 5.801	1.355 ± 0.081	1	22	< 1.271	0.4312 ± 0.0372	1	11
NGC4379	15.8	< 4.904	0.6206 ± 0.0433	1	22	< 1.824	0.2227 ± 0.0228	1	11
NGC4382	16.3	< 5.861	3.318 ± 0.160	2	22	< 2.044	1.157 ± 0.068	2	11
NGC4387	16.3	< 5.861	0.5031 ± 0.0386	2	22	< 1.349	0.1786 ± 0.0207	2	11
NGC4406	16.8	< 7.571	2.689 ± 0.135	8	22	< 4.292	0.8872 ± 0.0574	8	11
NGC4417	16.0	< 5.341	1.096 ± 0.065	1	22	< 1.138	0.3953 ± 0.0325	1	11
NGC4425	16.5	< 5.032	0.4629 ± 0.0370	1	22	< 1.163	0.1602 ± 0.0197	1	11
NGC4429	16.5	21.42 ± 1.57	7.004 ± 0.314	1	22	5.802 ± 0.591	2.651 ± 0.133	1	11
NGC4434	22.4	< 12.57	1.018 ± 0.076	1	22	< 3.835	0.3829 ± 0.0420	1	11
NGC4435	16.7	14.14 ± 1.26	5.667 ± 0.259	1	22	4.593 ± 0.556	2.386 ± 0.122	1	11
NGC4442	15.3	< 4.231	1.985 ± 0.102	1	22	< 1.952	0.7166 ± 0.0467	1	11
NGC4452	15.6	< 4.894	0.3095 ± 0.0276	1	22	< 0.9264	0.1040 ± 0.0148	1	11
NGC4458	16.3	< 5.861	0.3787 ± 0.0324	2	22	< 2.044	0.1391 ± 0.0180	2	11
NGC4459	16.3	33.62 ± 1.48	7.167 ± 0.321	2	22	11.03 ± 0.39	2.740 ± 0.136	2	11
NGC4461	16.5	< 5.048	1.271 ± 0.074	1	22	< 1.578	0.4677 ± 0.0370	1	11
NGC4472	17.1	< 5.608	5.214 ± 0.242	1	22	< 1.772	1.712 ± 0.094	1	11
NGC4473	16.3	< 3.856	2.434 ± 0.123	2	22	< 0.6940	0.8854 ± 0.0563	2	11
NGC4474	15.6	< 4.653	0.6562 ± 0.0446	1	22	< 1.704	0.2430 ± 0.0237	1	11
NGC4476	17.6	22.84 ± 2.28	3.536 ± 0.177	9	17.55				
NGC4477	16.3	6.478 ± 1.018	2.224 ± 0.114	2	22	4.395 ± 0.362	0.8049 ± 0.0526	2	11
NGC4478	17.0	< 6.097	1.157 ± 0.070	1	22	< 1.583	0.4039 ± 0.0345	1	11
NGC4483	16.7	< 5.090	0.4783 ± 0.0381	1	22	< 0.9158	0.1754 ± 0.0209	1	11
NGC4486	16.7	13.03 ± 1.26	6.088 ± 0.277	4	22	< 0.6940	1.966 ± 0.103	2	11
NGC4489	15.4	< 4.466	0.3452 ± 0.0292	1	22	< 1.485	0.1257 ± 0.0162	1	11
NGC4494	16.6	< 5.589	2.842 ± 0.141	1	22	< 1.473	1.078 ± 0.066	1	11
NGC4503	16.5	< 5.269	1.158 ± 0.069	1	22	< 1.017	0.4190 ± 0.0345	1	11
NGC4521	39.7	< 29.40	6.283 ± 0.380	1	22	< 7.832	2.522 ± 0.204	1	11
NGC4526	16.3	73.41 ± 2.34	13.04 ± 0.56	2	22	28.84 ± 0.56	4.821 ± 0.223	2	11
NGC4528	15.8	< 4.512	0.7315 ± 0.0486	1	22	< 1.059	0.2785 ± 0.0261	1	11
NGC4546	16.3	< 3.856	2.926 ± 0.144	2	22	< 1.349	1.100 ± 0.066	2	11
NGC4550	15.5	< 5.529	0.9541 ± 0.0580	1	22	< 1.993	0.3621 ± 0.0301	1	11
NGC4551	16.1	< 5.589	0.5709 ± 0.0417	1	22	< 1.864	0.2001 ± 0.0219	1	11
NGC4552	16.3	< 5.861	3.468 ± 0.167	2	22	< 1.349	1.233 ± 0.072	2	11
NGC4564	15.8	< 5.615	1.391 ± 0.078	1	22	< 1.803	0.5189 ± 0.0384	1	11
NGC4570	16.3	< 7.866	1.770 ± 0.095	2	22	< 2.044	0.6667 ± 0.0462	2	11
NGC4578	16.3	< 4.988	0.7295 ± 0.0494	1	22	< 2.154	0.2701 ± 0.0262	1	11
NGC4596	16.5	3.943 ± 0.930	2.773 ± 0.138	1	22	1.319 ± 0.309	1.061 ± 0.065	1	11
NGC4608	16.5	< 6.345	0.9470 ± 0.0596	1	22	< 1.420	0.3331 ± 0.0300	1	11
NGC4612	16.6	< 5.013	0.8249 ± 0.0543	1	22	< 1.325	0.3040 ± 0.0285	1	11
NGC4621	14.9	< 4.335	2.360 ± 0.117	1	22	< 0.6452	0.8445 ± 0.0518	1	11
NGC4623	17.4	< 5.173	0.4008 ± 0.0353	1	22	< 1.271	0.1424 ± 0.0194	1	11
NGC4624	16.5	< 6.329	1.379 ± 0.079	1	22	< 2.583	0.4647 ± 0.0368	1	11
NGC4636	13.6	< 0.7883	1.456 ± 0.076	3	22	0.200 ± 0.060	0.4858 ± 0.0332	3	11
NGC4638	17.5	< 6.354	1.572 ± 0.089	1	22	< 1.486	0.5799 ± 0.0443	1	11
NGC4643	16.5	< 7.611	2.475 ± 0.125	1	22	0.8790 ± 0.2816	0.9005 ± 0.0574	1	11
NGC4649	16.5	15.62 ± 1.95	14.71 ± 0.63	11	55	< 3.092	1.788 ± 0.098	1	11
NGC4660	15.0	< 4.982	1.357 ± 0.074	1	22	< 1.707	0.5224 ± 0.0372	1	11
NGC4684	13.1	3.080 ± 0.876	2.516 ± 0.119	1	22	3.086 ± 0.318	1.028 ± 0.056	1	11
NGC4690	40.2	< 32.87	1.852 ± 0.173	1	22	< 7.678	0.7318 ± 0.1015	1	11
NGC4694	16.5	19.56 ± 1.18	4.527 ± 0.211	1	22	5.195 ± 0.238	1.634 ± 0.090	1	11
NGC4697	11.4	< 2.304	1.786 ± 0.085	1	22	< 0.5079	0.6482 ± 0.0371	1	11
NGC4710	16.5	100.3 ± 2.9	10.31 ± 0.45	1	22	31.75 ± 0.61	3.561 ± 0.171	1	11
NGC4733	14.5	< 6.098	0.2358 ± 0.0222	1	22	< 0.9409	0.079 ± 0.012	1	11
NGC4753	22.9	68.08 ± 4.14	19.37 ± 0.85	1	22	21.64 ± 0.88	6.642 ± 0.320	1	11
NGC4754	16.1	< 4.806	1.760 ± 0.094	1	22	< 1.028	0.6063 ± 0.0430	1	11
NGC4762	22.6	< 9.529	2.704 ± 0.153	1	22	< 3.837	0.9407 ± 0.0725	1	11
NGC4803	39.4	< 30.40	1.187 ± 0.132	1	22	< 6.631	0.4531 ± 0.0772	1	11
NGC4839	102.0	< 118.5	13.34 ± 1.18	4	22	< 113.3	4.687 ± 0.649	4	11

Galaxy	D_L	$L_{\text{CO}(1-0)}$	$L_{12\mu\text{m}(1-0)}$	$\text{ref}_{(1-0)}$	$\text{Beam}_{(1-0)}$	$L_{\text{CO}(2-1)}$	$L_{12\mu\text{m}(2-1)}$	$\text{ref}_{(2-1)}$	$\text{Beam}_{(2-1)}$
(1)	(Mpc)	(10^6 [K km s $^{-1}$ pc $^{-2}$])	($10^7 L_{\odot}$)	(5)	(arcsec)	(10^6 [K km s $^{-1}$ pc $^{-2}$])	($10^7 L_{\odot}$)	(9)	(arcsec)
(2)	(3)	(4)	(6)	(7)	(8)	(10)			
NGC4874	102.0	< 92.78	15.70 \pm 1.31	4	22	< 58.16	5.422 \pm 0.703	4	11
NGC4889	102.0	< 108.8	27.92 \pm 1.90	4	22	< 46.45	10.13 \pm 1.00	4	11
NGC4914	74.5	< 42.20	17.16 \pm 1.12	4	22	< 19.90	6.316 \pm 0.584	4	11
NGC4956	70.9	< 26.67	15.29 \pm 1.00	3	22	< 8.333	5.406 \pm 0.512	3	11
NGC5103	23.4	< 12.19	1.114 \pm 0.083	1	22	< 2.267	0.4359 \pm 0.0467	1	11
NGC5173	38.4	36.58 \pm 4.94	8.829 \pm 0.485	1	22	13.32 \pm 0.98	3.497 \pm 0.247	1	11
NGC5198	36.3	< 19.16	3.076 \pm 0.219	2	22	< 3.448	1.098 \pm 0.116	2	11
NGC5208	105.0	514.8 \pm 21.7	77.27 \pm 4.11	4	22	121.1 \pm 6.0	29.06 \pm 1.98	4	11
NGC5252	103.8	< 128.3	301.5 \pm 13.5	4	22	< 74.12	134.9 \pm 6.5	4	11
NGC5273	16.1	3.926 \pm 0.681	2.662 \pm 0.132	1	22	2.493 \pm 0.153	1.111 \pm 0.066	1	11
NGC5308	28.3	< 17.70	2.971 \pm 0.183	2	22	< 8.151	1.072 \pm 0.093	2	11
NGC5322	30.3	< 18.20	8.741 \pm 0.440	1	22	< 5.056	3.204 \pm 0.201	1	11
NGC5342	35.5	< 19.41	1.154 \pm 0.117	1	22	< 4.798	0.3970 \pm 0.0647	1	11
NGC5353	35.4	38.79 \pm 5.68	11.41 \pm 0.58	3	22	29.00 \pm 2.00	4.268 \pm 0.270	3	11
NGC5355	37.1	< 27.44	2.729 \pm 0.205	1	22	< 11.74	1.142 \pm 0.120	1	11
NGC5358	38.0	< 26.60	0.5882 \pm 0.0864	1	22	< 7.658	0.2490 \pm 0.0545	1	11
NGC5379	30.0	40.95 \pm 3.61	4.626 \pm 0.263	1	22	8.042 \pm 1.595	1.713 \pm 0.130	1	11
NGC5422	30.8	< 19.24	2.831 \pm 0.186	1	22	< 8.656	1.082 \pm 0.100	1	11
NGC5444	60.5	< 23.33	10.04 \pm 0.68	3	22	< 10.00	3.787 \pm 0.364	3	11
NGC5473	33.2	< 22.36	5.737 \pm 0.325	1	22	< 7.639	2.256 \pm 0.167	1	11
NGC5475	28.6	< 16.78	1.979 \pm 0.139	1	22	< 4.564	0.7641 \pm 0.0766	1	11
NGC5481	25.8	< 12.57	0.9325 \pm 0.0797	1	22	< 4.362	0.3450 \pm 0.0447	1	11
NGC5485	25.2	< 12.62	3.280 \pm 0.186	1	22	< 2.934	1.108 \pm 0.087	1	11
NGC5490	71.9	< 23.33	13.69 \pm 0.93	3	22	< 11.67	5.255 \pm 0.509	3	11
NGC5493	38.8	< 30.36	7.779 \pm 0.442	1	22	< 8.071	2.942 \pm 0.222	1	11
NGC5500	31.7	< 21.20	0.5231 \pm 0.0679	1	22	< 6.249	0.1914 \pm 0.0396	1	11
NGC5507	28.5	< 15.77	2.001 \pm 0.140	1	22	< 2.915	0.7708 \pm 0.0769	1	11
NGC5557	38.8	< 26.25	7.055 \pm 0.410	1	22	< 5.206	2.573 \pm 0.204	1	11
NGC5574	23.2	< 10.23	1.064 \pm 0.080	1	22	< 2.252	0.3728 \pm 0.0425	1	11
NGC5576	24.8	< 12.65	3.627 \pm 0.200	1	22	< 2.431	1.364 \pm 0.098	1	11
NGC5582	27.7	< 14.98	1.554 \pm 0.116	1	22	< 3.055	0.5830 \pm 0.0637	1	11
NGC5611	24.5	< 11.79	1.024 \pm 0.081	1	22	< 3.079	0.4118 \pm 0.0471	1	11
NGC5629	67.7	< 33.33	8.618 \pm 0.660	3	22	< 15.00	3.221 \pm 0.364	3	11
NGC5631	27.0	< 15.13	3.978 \pm 0.223	1	22	< 3.612	1.384 \pm 0.105	1	11
NGC5638	25.6	< 12.61	2.212 \pm 0.140	1	22	< 2.390	0.7796 \pm 0.0708	1	11
NGC5687	27.2	< 13.89	1.667 \pm 0.120	1	22	< 2.806	0.6362 \pm 0.0660	1	11
NGC5770	18.5	< 6.902	0.7397 \pm 0.0540	1	22	< 1.517	0.2796 \pm 0.0297	1	11
NGC5813	29.9	< 3.333	4.283 \pm 0.248	3	22	< 5.327	1.148 \pm 0.092	2	11
NGC5831	22.8	< 15.41	1.689 \pm 0.108	2	22	< 4.003	0.6169 \pm 0.0561	2	11
NGC5838	18.7	< 7.731	4.388 \pm 0.212	2	22	< 2.696	1.755 \pm 0.100	2	11
NGC5839	22.0	< 7.567	1.059 \pm 0.077	1	22	< 1.526	0.3899 \pm 0.0416	1	11
NGC584	18.7	< 3.333	2.839 \pm 0.147	3	22	< 0.8333	1.026 \pm 0.068	3	11
NGC5845	21.8	< 6.892	1.922 \pm 0.116	2	22	< 1.241	0.8068 \pm 0.0639	2	11
NGC5846	23.1	2.838 \pm 0.946	3.716 \pm 0.198	3	22	0.8000 \pm 0.2000	1.222 \pm 0.087	3	11
NGC5854	26.2	< 12.53	1.850 \pm 0.126	1	22	< 2.244	0.6632 \pm 0.0656	1	11
NGC5864	29.0	< 17.30	1.848 \pm 0.134	1	22	< 4.387	0.6256 \pm 0.0691	1	11
NGC5866	14.9	55.77 \pm 1.34	6.736 \pm 0.299	6	22	< 1074.2	2.309 \pm 0.114	6	11
NGC5869	24.9	< 13.55	1.704 \pm 0.115	1	22	< 2.856	0.6335 \pm 0.0612	1	11
NGC5982	41.9	< 13.25	8.307 \pm 0.481	2	22	< 4.587	3.074 \pm 0.241	2	11
NGC6010	30.6	< 19.16	2.782 \pm 0.184	1	22	< 3.701	1.063 \pm 0.099	1	11
NGC6014	35.8	111.5 \pm 6.4	15.80 \pm 0.76	1	22	39.97 \pm 1.54	6.496 \pm 0.370	1	11
NGC6017	29.0	< 16.96	5.047 \pm 0.277	1	22	< 3.458	2.170 \pm 0.149	1	11
NGC6149	37.2	< 25.09	2.347 \pm 0.187	1	22	< 7.118	0.9489 \pm 0.1088	1	11
NGC6278	42.9	< 30.70	5.402 \pm 0.357	1	22	< 8.958	2.143 \pm 0.196	1	11
NGC6482	61.4	< 24.14	17.57 \pm 1.02	4	22	< 7.198	6.504 \pm 0.513	4	11
NGC6547	40.8	< 32.12	3.621 \pm 0.264	1	22	< 10.11	1.441 \pm 0.149	1	11
NGC6548	33.6	< 24.89	3.779 \pm 0.240	2	22	< 17.19	1.403 \pm 0.125	2	11
NGC6658	64.0	< 25.00	7.522 \pm 0.581	3	22	< 8.333	2.944 \pm 0.330	3	11
NGC6703	25.9	< 13.41	3.040 \pm 0.178	1	22	< 5.487	1.122 \pm 0.089	1	11
NGC6798	37.5	13.00 \pm 3.35	4.447 \pm 0.287	1	22	< 4.168	1.550 \pm 0.145	1	11

Galaxy	D_L	$L_{CO(1-0)}$	$L_{12\mu m(1-0)}$	$ref_{(1-0)}$	$Beam_{(1-0)}$	$L_{CO(2-1)}$	$L_{12\mu m(2-1)}$	$ref_{(2-1)}$	$Beam_{(2-1)}$
(1)	(Mpc)	(10^6 [K km s $^{-1}$ pc $^{-2}$])	($10^7 L_\odot$)	(5)	(arcsec)	(10^6 [K km s $^{-1}$ pc $^{-2}$])	($10^7 L_\odot$)	(9)	(arcsec)
(2)	(3)	(4)	(6)	(7)	(8)	(10)			
NGC7052	69.3	42.43 ± 8.93	28.87 ± 1.58	4	22	8.094 ± 2.233	11.99 ± 0.83	4	11
NGC7265	82.8	< 69.30	18.12 ± 1.24	4	22	< 46.32	6.635 ± 0.656	4	11
NGC7274	82.8	< 45.43	13.16 ± 1.00	4	22	< 13.61	4.833 ± 0.547	4	11
NGC7280	23.7	< 9.728	1.968 ± 0.124	1	22	< 2.228	0.7734 ± 0.0664	1	11
NGC7332	22.4	< 8.253	3.178 ± 0.172	1	22	< 1.888	1.206 ± 0.085	1	11
NGC7454	23.2	< 7.821	0.9216 ± 0.0732	1	22	< 2.119	0.3375 ± 0.0402	1	11
NGC7457	12.9	< 2.892	0.4349 ± 0.0298	1	22	< 0.6553	0.1503 ± 0.0153	1	11
NGC7465	29.3	118.6 ± 4.5	37.54 ± 1.63	1	22	53.19 ± 1.19	14.89 ± 0.69	1	11
NGC7550	72.7	117.5 ± 12.5	22.97 ± 1.36	4	22	69.19 ± 6.66	8.950 ± 0.711	4	11
NGC7556	103.0	< 51.24	17.81 ± 1.43	4	22	< 21.15	5.575 ± 0.722	4	11
NGC7618	76.3	< 43.29	14.75 ± 1.02	4	22	< 27.45	5.592 ± 0.554	4	11
NGC7619	54.3	< 10.00	14.21 ± 0.82	3	22	< 6.667	5.279 ± 0.411	3	11
NGC7626	54.0	< 42.91	11.79 ± 0.71	4	22				
NGC7693	35.4	< 23.31	0.5464 ± 0.0797	1	22	< 5.663	0.2048 ± 0.0468	1	11
NGC7710	34.0	< 19.89	1.026 ± 0.107	1	22	< 5.896	0.3960 ± 0.0626	1	11
NGC924	63.6	< 37.84	8.783 ± 0.641	3	22	11.00 ± 2.00	3.269 ± 0.349	3	11
NGC978	68.7	< 25.00	11.88 ± 0.83	3	22	< 6.667	4.409 ± 0.443	3	11
PGC016060	37.8	34.96 ± 5.26	8.130 ± 0.452	1	22	6.897 ± 1.507	2.814 ± 0.212	1	11
PGC028887	41.0	< 33.80	0.6769 ± 0.1023	1	22	< 15.68	0.3158 ± 0.0671	1	11
PGC029321	40.9	64.85 ± 5.52	51.44 ± 2.28	1	22	23.15 ± 1.44	22.33 ± 1.07	1	11
PGC035754	39.0	< 25.19	0.8113 ± 0.1057	1	22	< 7.912	0.3358 ± 0.0653	1	11
PGC042549	40.7	< 37.35	3.980 ± 0.281	1	22	< 7.100	1.455 ± 0.150	1	11
PGC044433	40.1	< 30.65	1.154 ± 0.132	1	22	< 7.687	0.4815 ± 0.0810	1	11
PGC050395	37.2	< 23.65	0.7030 ± 0.0927	1	22	< 5.509	0.2787 ± 0.0563	1	11
PGC051753	38.3	< 26.26	0.7777 ± 0.1008	1	22	< 6.692	0.3041 ± 0.0607	1	11
PGC054452	29.5	< 16.94	0.4181 ± 0.0570	1	22	< 4.653	0.1550 ± 0.0335	1	11
PGC056772	39.5	29.38 ± 3.65	12.64 ± 0.65	1	22	9.290 ± 0.920	5.557 ± 0.347	1	11
PGC058114	23.8	75.22 ± 2.96	19.89 ± 0.87	1	22	35.37 ± 0.52	8.522 ± 0.402	1	11
PGC061468	36.2	19.19 ± 3.21	4.194 ± 0.270	1	22	3.614 ± 0.815	1.761 ± 0.153	1	11
PGC071531	30.4	< 14.07	0.6711 ± 0.0762	1	22	< 2.766	0.2631 ± 0.0454	1	11
PGC170172	37.1	< 29.84	0.7494 ± 0.0973	1	22	< 7.520	0.3047 ± 0.0595	1	11
PGC32543	9.1	0.5771 ± 0.1367	0.4585 ± 0.0256	5	22	0.5714 ± 0.0910	0.1613 ± 0.0122	5	11
PGC35225	14.8	0.5672 ± 0.1215	0.5018 ± 0.0360	5	22	0.5126 ± 0.0540	0.1912 ± 0.0198	5	11
PGC36686	10.7	1.258 ± 0.168	1.073 ± 0.054	5	22	0.7191 ± 0.0977	0.3814 ± 0.0242	5	11
PGC44685	12.5	0.6644 ± 0.1733	0.9176 ± 0.0506	5	22	0.2693 ± 0.0577	0.3740 ± 0.0264	5	11
UGC03960	33.2	< 20.37	0.4658 ± 0.0689	1	22	< 7.703	0.1541 ± 0.0382	1	11
UGC04551	28.0	< 13.31	1.822 ± 0.130	1	22	< 5.707	0.7384 ± 0.0739	1	11
UGC05408	45.8	39.82 ± 6.32	30.13 ± 1.43	1	22	20.78 ± 1.47	12.63 ± 0.69	1	11
UGC06062	38.7	< 27.33	1.664 ± 0.158	1	22	< 7.965	0.6009 ± 0.0882	1	11
UGC06176	40.1	73.23 ± 7.10	29.57 ± 1.37	1	22	39.73 ± 2.13	12.42 ± 0.65	1	11
UGC08876	33.9	< 19.97	1.184 ± 0.114	1	22	< 5.110	0.4672 ± 0.0675	1	11
UGC09519	27.6	112.1 ± 3.9	6.247 ± 0.322	1	22	30.67 ± 0.72	2.562 ± 0.162	1	11
ESO507-25	45.2					92.00 ± 12.00	19.32 ± 0.97	3	27
NGC1395	22.4					< 10.00	5.800 ± 0.283	3	27
NGC1779	44.4					99.00 ± 13.00	23.65 ± 1.15	3	27
NGC2292	29.6					< 16.67	2.536 ± 0.169	3	27
NGC3078	32.7					< 8.333	9.806 ± 0.496	3	27
NGC3923	21.3					< 10.00	5.812 ± 0.280	3	27
NGC5061	28.3					< 15.00	10.55 ± 0.51	3	27
NGC5084	24.1					< 5.000	8.752 ± 0.413	3	27
NGC5153	60.5					< 63.33	9.002 ± 0.631	3	27
NGC5903	31.5					< 21.67	4.675 ± 0.272	3	27
NGC7377	46.7					103.0 ± 10.0	21.36 ± 1.07	3	27

NOTE— Notes: (1) Object name, (2) the galaxy distances, (3) CO(1-0) luminosities (and uncertainties) from the paper referenced in Column (5), (4) *WISE* 12 μm luminosities in CO(1-0) beams listed in Column (6). Column 7–10 are as Column 3–6, but for the CO(2-1) line observations. References: 1; Young et al. (2011), 2; Combes et al. (2007), 3; O’Sullivan et al. (2018), 4; observations of MASSIVE galaxies with IRAM (Davis & Bureau 2016; Davis et al. 2019; Ocaña Flaquer et al. 2010; O’Sullivan et al. 2015; Wiklind et al. 1995), 5; Ge et al. (2021), 6, Welch & Sage (2003), 7, Sage et al. (2007), 8, Wiklind et al. (1995), 9, Young (2002), 10, Welch et al. (2010), 11, Georgakakis et al. (2001), 12, Knapp & Rupen (1996), 13, Young (2005), 14, provided by Davis privately.

REFERENCES

- Accurso, G., Saintonge, A., Catinella, B., et al. 2017, *MNRAS*, 470, 4750
- Baan, W. A., Henkel, C., Loenen, A. F., Baudry, A., & Wiklind, T. 2008, *A&A*, 477, 747
- Baldry, I. K., Glazebrook, K., Brinkmann, J., et al. 2004, *ApJ*, 600, 681
- Bendo, G. J., Lu, N., & Zijlstra, A. 2020, *MNRAS*, 496, 1393
- Bendo, G. J., Draine, B. T., Engelbracht, C. W., et al. 2008, *MNRAS*, 389, 629
- Bendo, G. J., Wilson, C. D., Warren, B. E., et al. 2010, *MNRAS*, 402, 1409
- Bertemes, C., Wuyts, S., Lutz, D., et al. 2018, *MNRAS*, 478, 1442
- Bertin, E., & Arnouts, S. 1996, *A&AS*, 117, 393
- Bigiel, F., Leroy, A., Walter, F., et al. 2008, *AJ*, 136, 2846
- Blanton, M. R., Kazin, E., Muna, D., Weaver, B. A., & Price-Whelan, A. 2011, *AJ*, 142, 31
- Bolatto, A. D., Wolfire, M., & Leroy, A. K. 2013, *ARA&A*, 51, 207
- Boquien, M., Kennicutt, R., Calzetti, D., et al. 2016, *A&A*, 591, A6
- Cappellari, M., Emsellem, E., Krajnović, D., et al. 2011, *MNRAS*, 413, 813
- Chastenet, J., Sandstrom, K., Chiang, I.-D., et al. 2019, *ApJ*, 876, 62
- Chown, R., Li, C., Parker, L., et al. 2021, *MNRAS*, 500, 1261
- Chown, R., Leroy, A. K., Sandstrom, K., et al. 2024, arXiv e-prints, arXiv:2410.05397
- Churchwell, E., Povich, M. S., Allen, D., et al. 2006, *ApJ*, 649, 759
- Colombo, D., Kalinova, V., Utomo, D., et al. 2018, *MNRAS*, 475, 1791
- Combes, F., Young, L. M., & Bureau, M. 2007, *MNRAS*, 377, 1795
- Cortzen, I., Garrett, J., Magdis, G., et al. 2019, *MNRAS*, 482, 1618
- Davis, T. A., & Bureau, M. 2016, *MNRAS*, 457, 272
- Davis, T. A., Greene, J. E., Ma, C.-P., et al. 2019, *MNRAS*, 486, 1404
- Davis, T. A., Alatalo, K., Bureau, M., et al. 2013, *MNRAS*, 429, 534
- Davis, T. A., Young, L. M., Crocker, A. F., et al. 2014, *MNRAS*, 444, 3427
- de Vaucouleurs, G., de Vaucouleurs, A., Corwin, Herold G., J., et al. 1991, *Third Reference Catalogue of Bright Galaxies*
- den Brok, J. S., Chatzigiannakis, D., Bigiel, F., et al. 2021, *MNRAS*, 504, 3221
- Diamond-Stanic, A. M., & Rieke, G. H. 2010, *ApJ*, 724, 140
- Donoso, E., Yan, L., Tsai, C., et al. 2012, *ApJ*, 748, 80
- Draine, B. T., & Li, A. 2007, *ApJ*, 657, 810
- Gao, Y., & Solomon, P. M. 2004a, *ApJS*, 152, 63
- . 2004b, *ApJ*, 606, 271
- Gao, Y., Tan, Q.-H., Gao, Y., et al. 2022, *ApJ*, 940, 133
- Gao, Y., Xiao, T., Li, C., et al. 2019, *ApJ*, 887, 172
- Ge, X., Gu, Q.-S., García-Benito, R., et al. 2021, *MNRAS*, 507, 4262
- Georgakakis, A., Hopkins, A. M., Caulton, A., et al. 2001, *MNRAS*, 326, 1431
- Gong, M., Ostriker, E. C., Kim, C.-G., & Kim, J.-G. 2020, *ApJ*, 903, 142
- Huchra, J. P., Macri, L. M., Masters, K. L., et al. 2012, *ApJS*, 199, 26
- Hudgins, D. M., & Allamandola, L. J. 2005, in *Astrochemistry: Recent Successes and Current Challenges*, ed. D. C. Lis, G. A. Blake, & E. Herbst, Vol. 231, 443–454
- Hunt, L. K., De Looze, I., Boquien, M., et al. 2019, *A&A*, 621, A51
- Jarrett, T. H., Cohen, M., Masci, F., et al. 2011, *The Astrophysical Journal*, 735, 112
- Jiang, X.-J., Wang, Z., Gu, Q., Wang, J., & Zhang, Z.-Y. 2015, *ApJ*, 799, 92
- Jing, T., & Li, C. 2024, arXiv e-prints, arXiv:2411.08747
- Kaneda, H., Onaka, T., Sakon, I., et al. 2008, *ApJ*, 684, 270
- Kauffmann, G., Heckman, T. M., De Lucia, G., et al. 2006, *MNRAS*, 367, 1394
- Kaviraj, S., Schawinski, K., Devriendt, J. E. G., et al. 2007, *ApJS*, 173, 619
- Kelly, B. C. 2007, *ApJ*, 665, 1489
- Kennicutt, Robert C., J. 1998, *ApJ*, 498, 541
- Kim, J., Chevance, M., Kruijssen, J. M. D., et al. 2022, *MNRAS*, 516, 3006
- Knapp, G. R., & Rupen, M. P. 1996, *ApJ*, 460, 271
- Koda, J., Sawada, T., Sakamoto, K., et al. 2020, *ApJL*, 890, L10
- Krumholz, M. R., & McKee, C. F. 2005, *ApJ*, 630, 250
- Landsman, W. B. 1995, in *Astronomical Society of the Pacific Conference Series*, Vol. 77, *Astronomical Data Analysis Software and Systems IV*, ed. R. A. Shaw, H. E. Payne, & J. J. E. Hayes, 437
- Leroy, A. K., Walter, F., Brinks, E., et al. 2008, *AJ*, 136, 2782
- Leroy, A. K., Bolatto, A., Gordon, K., et al. 2011, *ApJ*, 737, 12
- Leroy, A. K., Bigiel, F., de Blok, W. J. G., et al. 2012, *AJ*, 144, 3
- Leroy, A. K., Walter, F., Sandstrom, K., et al. 2013, *AJ*, 146, 19
- Leroy, A. K., Sandstrom, K. M., Lang, D., et al. 2019, *ApJS*, 244, 24
- Leroy, A. K., Rosolowsky, E., Usero, A., et al. 2022, *ApJ*, 927, 149
- Leroy, A. K., Bolatto, A. D., Sandstrom, K., et al. 2023a, *ApJL*, 944, L10
- Leroy, A. K., Sandstrom, K., Rosolowsky, E., et al. 2023b, *ApJL*, 944, L9
- Li, A. 2020, *Nature Astronomy*, 4, 339
- Li, C., Kauffmann, G., Fu, J., et al. 2012, *MNRAS*, 424, 1471
- Ma, C.-P., Greene, J. E., McConnell, N., et al. 2014, *ApJ*, 795, 158
- Meijerink, R., & Spaans, M. 2005, *A&A*, 436, 397

- Ocaña Flaquer, B., Leon, S., Combes, F., & Lim, J. 2010, *A&A*, 518, A9
- O’Sullivan, E., Combes, F., Hamer, S., et al. 2015, *A&A*, 573, A111
- O’Sullivan, E., Forbes, D. A., & Ponman, T. J. 2001, *MNRAS*, 328, 461
- O’Sullivan, E., Combes, F., Salomé, P., et al. 2018, *A&A*, 618, A126
- Pan, H.-A., Schinnerer, E., Hughes, A., et al. 2022, *ApJ*, 927, 9
- Peng, Y.-j., Lilly, S. J., Kovač, K., et al. 2010, *ApJ*, 721, 193
- Rieke, G. H., Wright, G. S., Böker, T., et al. 2015, *PASP*, 127, 584
- Ronayne, K., Papovich, C., Yang, G., et al. 2024, *ApJ*, 970, 61
- Sage, L. J., Welch, G. A., & Young, L. M. 2007, *ApJ*, 657, 232
- Saintonge, A., & Catinella, B. 2022, *ARA&A*, 60, 319
- Sakamoto, S., Hayashi, M., Hasegawa, T., Handa, T., & Oka, T. 1994, *ApJ*, 425, 641
- Salpeter, E. E. 1955, *ApJ*, 121, 161
- Sanders, D. B., & Mirabel, I. F. 1996, *ARA&A*, 34, 749
- Sandstrom, K. M., Bolatto, A. D., Draine, B. T., Bot, C., & Stanimirović, S. 2010, *ApJ*, 715, 701
- Sandstrom, K. M., Bolatto, A. D., Bot, C., et al. 2012, *ApJ*, 744, 20
- Sandstrom, K. M., Koch, E. W., Leroy, A. K., et al. 2023, *ApJL*, 944, L8
- Shivaei, I., & Boogaard, L. A. 2024, *A&A*, 691, L2
- Smith, J. D. T., Draine, B. T., Dale, D. A., et al. 2007, *ApJ*, 656, 770
- Solomon, P. M., Rivolo, A. R., Barrett, J., & Yahil, A. 1987, *ApJ*, 319, 730
- Tacconi, L. J., Genzel, R., & Sternberg, A. 2020, *ARA&A*, 58, 157
- Temì, P., Brighenti, F., & Mathews, W. G. 2009, *ApJ*, 695, 1
- Tielens, A. G. G. M. 2008, *ARA&A*, 46, 289
- Villaume, A., Conroy, C., & Johnson, B. D. 2015, *ApJ*, 806, 82
- Visser, R., van Dishoeck, E. F., & Black, J. H. 2009, *A&A*, 503, 323
- Walterbos, R. A. M., & Schwering, P. B. W. 1987, *A&A*, 180, 27
- Watson, C., Povich, M. S., Churchwell, E. B., et al. 2008, *ApJ*, 681, 1341
- Welch, G. A., & Sage, L. J. 2003, *ApJ*, 584, 260
- Welch, G. A., Sage, L. J., & Young, L. M. 2010, *ApJ*, 725, 100
- Whitcomb, C. M., Sandstrom, K., Leroy, A., & Smith, J. D. T. 2023, *ApJ*, 948, 88
- Wiklind, T., Combes, F., & Henkel, C. 1995, *A&A*, 297, 643
- WISE Team. 2020, *AllWISE Atlas (L3a) Coadd Images*, IPAC, doi:10.26131/IRSA153. <https://catcopy.ipac.caltech.edu/doi/doi.php?id=10.26131/IRSA153>
- Wolfire, M. G., Hollenbach, D., & McKee, C. F. 2010, *ApJ*, 716, 1191
- Wolfire, M. G., Vallini, L., & Chevance, M. 2022, *ARA&A*, 60, 247
- Wright, E. L., Eisenhardt, P. R. M., Mainzer, A. K., et al. 2010, *AJ*, 140, 1868
- Yajima, Y., Sorai, K., Miyamoto, Y., et al. 2021, *PASJ*, 73, 257
- Yi, S. K., Yoon, S. J., Kaviraj, S., et al. 2005, *ApJL*, 619, L111
- Young, L. M. 2002, *AJ*, 124, 788
- . 2005, *ApJ*, 634, 258
- Young, L. M., Bureau, M., Davis, T. A., et al. 2011, *MNRAS*, 414, 940
- Zhang, L., & Ho, L. C. 2023, *ApJ*, 943, 60